Liquid-vapor transformations with surfactants. Phase-field model and Isogeometric Analysis

Jesus Bueno[1], Hector Gomez

Departamento de Métodos Matemáticos e de Representación. Universidade da Coruña.
Campus de Elviña, 15192, A Coruña, Spain

Abstract

Surfactants are compounds that find energetically favorable to be located at the boundaries between fluids. They are able to modify the properties of those interfaces, for example, reducing surface tension. Here, we propose a new model for liquid-vapor flows with surfactants which captures the dynamics of the surfactant and accounts for phase transformations in the fluid. The aforementioned model is derived from a free energy functional by using a Coleman-Noll approach. The proposed theory emanates from the isothermal Navier-Stokes-Korteweg equations, which describe single-component two-phase flow and naturally allow for phase transformations. We believe that our model has significant potential to study the influence of surfactants in vaporization and condensation processes. From a numerical point of view, the proposed model poses significant challenges to existing discretization methods, including stiffness in space and time, internal and boundary layers as well as higher-order partial differential operators. To overcome these challenges we propose algorithms based on Isogeometric Analysis, which permit an accurate and efficient discretization. Finally, we illustrate the viability of the theoretical framework and the effectiveness of our algorithms by solving several numerical problems in two and three dimensions.

Keywords: Surfactants, Surface tension, Navier-Stokes-Korteweg (NSK), Complex fluids, Phase-field model, Isogeometric Analysis (IGA).

1. Introduction

Surfactants are very useful products in the chemical industry. They can be found in detergents, cosmetics, or the dye of our clothes. However, the chemical industry is not the only beneficiary of these extraordinary compounds. In recent decades, surfactants have also been used in other fields such as biotechnology [1, 2], electronic printing [3], microelectronics [4] or medical research [5, 6]. They also play an essential role in our organism, increasing the pulmonary compliance and preventing atelectasis [7, 8], that is, the complete or the partial collapse of the lungs.

The word surfactant is an abbreviation of *surface active agent* and is used to name different types of compounds that find energetically favorable to be located at the interfaces of a system. The consequence is that surfactants are absorbed by the interface, that is, they get trapped at the boundary between different phases. Even if they are usually very thin, interfaces play a crucial role in the system dynamics. The composition in the interfacial region can differ dramatically from that of the bulk phases. Indeed, across interfaces there are rapid property changes that lead to an excess of free energy, related to the amount of work required to create the interface. The presence of surfactants at the interface can significantly reduce the work required to generate interfaces, altering completely the behavior of the system [9–13]. For a more detailed discussion on surfactant properties the reader is referred to [14–16]

In the literature, one can find a number of computational methods that describe surfactant absorption phenomena. For this purpose, different techniques have been employed, such as phase-field models [17–21], front tracking methods [19, 22] or volume of fluid schemes [23, 24]. However, most of these models only deal with soluble or insoluble

[1]E-mail: jesus.bueno@udc.es

surfactants in two-component inmiscible flows (see, for example, [25–27]). The influence of surfactants in single-component two-phase flows remains practically unexplored, at least from the computational point of view. For this reason, we present our initial steps toward a computational model for surfactants that tries to capture the behavior and the effects of surface active agents at the interfaces of single component flows. The proposed model is based on a complex-fluid theory that allows for spontaneous vaporization and condensation, so it may have a significant potential to study the influence of surfactants in phase-transition phenomena.

1.1. Fluid dynamics with phase changes

There exist two different approaches to deal with phase transformations: sharp-interface and diffuse interface models. The former usually results in mathematical models that require complex numerical treatment: one must solve simultaneously the partial differential equations that govern each phase's dynamics as well as the boundary conditions that hold on a moving, and *a priori* unknown, interface [28]. An alternative to the previous approach is the diffuse-interface method in which sharp interfaces are replaced by thin transition regions. The idea is to define an order parameter, also called phase-field, that varies smoothly on the entire computational domain and acts as marker of the location of the different phases. This notably simplifies the numerics because the governing equations can be solved on the entire domain, which is usually known and fixed. In general, instead of the boundary conditions at the interfaces, we have to solve a partial differential equation for the evolution of the order parameter. From the computational point of view, the main disadvantage is that this equation typically includes higher-order partial-differential operators, and it produces thin layers that evolve dynamically over the computational domain. However, most of these computational challenges are being addressed [29–32], and in recent decades phase-field models have been successfully applied to a large number of fields such as solidification dynamics [33–35], foams [36], fracture dynamics [37], dendritic growth [38, 39], vesicle dynamics [40], microstructure evolution in solids [41], planet formation [42], infiltration of water into a porous medium [43, 44], coalescence of bubbles [45], cancer growth [46–48], elasto-capillarity [49] or fluid-structure interaction [50]. For recent reviews of phase-field methods the reader is referred to [51–55].

To develop our theory of liquid-vapor flows with surfactants, we use as a starting point the Navier-Stokes-Korteweg (NSK) equations, which are a phase-field theory for single-component two-phase flows [45]. The model allows for the fluid to evaporate and condensate naturally due to pressure and/or temperature variations. An interesting feature of the model is that the fluid density acts directly as the phase-field identifying the liquid and vapor phases. The NSK system is the result of several works, including the contributions of Gibbs [56], Korteweg [57], van der Waals [58] and Dunn and Serrin [59]. Although the current form of the system has been known for several years, computational methods for the NSK equations are still in their infancy. Some noteworthy publications are, for example, [32, 45, 60–63].

Including surfactants in the theory makes the computational treatment even more difficult. Since surfactants tend to be located primarily on the interfaces, a common approach is to model surfactant dynamics as a partial-differential equation that is posed on the lower-dimensional manifold defined by the interface. Our goal is to adhere to the phase-field philosophy also to model the surfactant dynamics and define a global field which naturally localizes to the interface. This leads to a much simpler computational treatment.

1.2. Computational challenges

One of the main challenges when dealing with phase-field approaches or in particular with the Navier-Stokes-Korteweg equations, is that these models include a length scale that represents the thickness of the interfaces, which must be extremely small in order for the model to be realistic. This interface length scale must be captured by the computational mesh, which makes the NSK theory more difficult to treat numerically than classical Navier-Stokes equations. Additionally, our model involves third-order partial-differential spatial operators both in the NSK system and in the equation that describes the behavior of the surfactant. This fact significantly limits the use of finite element methods since we need to employ basis functions with $\mathcal{C}^1$ global continuity, which is very difficult or even impossible in 3D complicated geometries.

The aforementioned difficulties are tackled by using Isogeometric Analysis (IGA) for the spatial discretization of the problem. IGA is a new computational technique that improves and generalizes the standard finite element method. It was first proposed in [64] and further developed in [65–69]. The main objective of IGA is to bridge the gap between Computer Aided Design (CAD) and Finite Element Analysis by developing a computational framework based on the functions employed in CAD systems. There are a number of computational geometry technologies that may be

used in Isogeometric Analysis. Heretofore, Non-Uniform Rational B-Splines (NURBS) have been the functions most widely employed in IGA, and they will also be used for our simulations. However, there are other options such as T-Splines (see, for example, [66, 70, 71]) or subdivision surfaces [72]. Isogeometric analysis based on NURBS presents a series of attributes that can be exploited in problems involving higher-order partial-differential operators. Among them, it is worth highlighting the following: higher-order accuracy, robustness, and especially, higher-order global continuity of the basis functions. IGA has been previously used to solve phase-field problems with remarkable success [29, 31, 45, 50, 73–76]. Another important property of IGA that has been recently proven is that Galerkin solutions can be obtained with only one evaluation per degree of freedom using the concept of variational collocation [77].

1.3. Structure and content of the paper

The rest of the paper is organized as follows. Section 2 gives a quick overview of Isogeometric Analysis based on NURBS. In Section 3, we derive our model from a free energy functional by using a Coleman-Noll approach [78]. In Section 4, we describe the governing equations of the model at the continuous level. Then, we present the weak form of the problem as well as the discretization process. We employ a semi-discrete formulation based on Galerkin's method and we integrate in time using a generalized-α scheme [79]. Section 5 displays several numerical examples in 2D and 3D. The first example aims at finding the relation between the surface tension at liquid-vapor interfaces and the parameters of the proposed model. It also shows that our theory succeeds in reproducing the way in which surfactants lower surface tension. The second simulation demonstrates that surfactants are naturally trapped at interfaces in accordance with the expected physical behavior of a surface active agent. We also use this example to show that our model is able to reproduce how surfactants may inhibit the coalescence of bubbles. For this particular case, we plot the evolution of the free energy with respect to time, and we confirm that it decreases monotonically as it was imposed in the derivation of the theory. Subsequently, we present a numerical example in which a drop of water is attracted by a solid-like boundary due to the capillarity forces associated to the liquid-vapor interfaces. The contact angle between those interfaces and the boundary will be altered because of the surfactant concentration. Additionally, a three-dimensional numerical simulation is presented. Finally, in Section 6, some concluding remarks are commented.

2. A brief overview of NURBS-based Isogeometric Analysis

The current implementation of our IGA model is based on Non-Uniform Rational B-Splines (NURBS). The goal of this section is to introduce NURBS briefly and to present a quick overview of Isogeometric Analysis. For a more extensive discussion on IGA the reader is referred to [80].

B-splines are piecewise polynomial curves constructed by taking linear combinations of B-spline basis functions. The coefficients of these basis are points in space, which are referred to as *control points*. The concept is similar to that of nodal coordinates in finite element analysis. The only difference is that in IGA the basis functions are, in general, non-interpolatory. A *knot vector* Ξ in one dimension is a set of non-decreasing coordinates in the parametric space, i.e., $\Xi = \{\xi_1, ..., \xi_{n_c+p+1}\}$, where $\xi_i \in \mathbb{R}$ is the ith knot, $i = 1, 2, ..., n_c + p + 1$, p is the polynomial order, and n_c is the number of basis functions that comprise the B-spline space. Knots divide the parametric space into knot spans or elements.

For a given knot vector, the B-spline basis functions are defined by the *Cox-de Boor recursion formula* (see [81], [82]). This way, starting with piecewise constants ($p = 0$), i.e,

$$N_{i,0}(\xi) = \begin{cases} 1, & \text{if } \xi_i \leqslant \xi < \xi_{i+1}, \\ 0, & \text{otherwise} \end{cases}; \quad i = 1, \ldots, n_c \tag{1}$$

the basis functions of higher degrees are defined by

$$N_{i,p}(\xi) = \frac{\xi - \xi_i}{\xi_{i+p} - \xi_i} N_{i,p-1}(\xi) + \frac{\xi_{i+p+1} - \xi}{\xi_{i+p+1} - \xi_{i+1}} N_{i+1,p-1}(\xi); \quad i = 1, \ldots, n_c \tag{2}$$

Note that for B-spline functions with polynomial order 0 and 1, we obtain standard piecewise constant and linear finite element functions, respectively. From the Cox-de Boor recursion formula, it can be seen that B-Spline basis functions

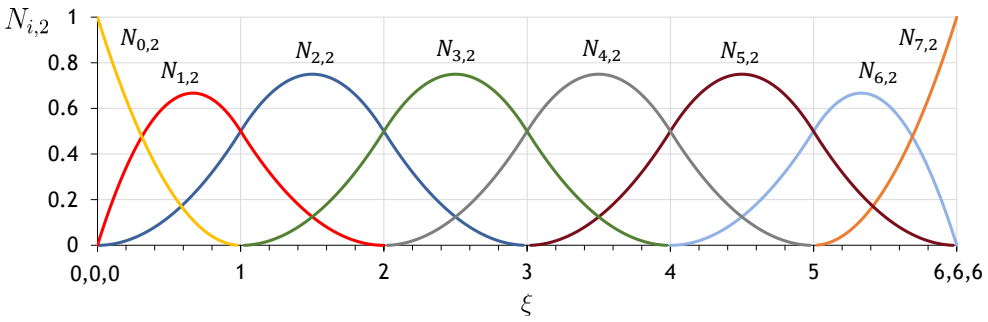

Figure 1: Quadratic basis functions formed from the open knot vector $\Xi = \{0, 0, 0, 1, 2, 3, 4, 5, 6, 6, 6\}$

constitute a partition of unity, that is, $\sum_{i=1}^{n_c} N_{i,p}(\xi) = 1 \; \forall \xi$. Moreover, each basis $N_{i,p}$ is pointwise nonnegative over the entire domain, i.e., $N_{i,p}(\xi) \geqslant 0 \; \forall \xi$, and its support is compact. For B-spline functions of order p the support is always $p+1$ knot spans. It is also important to note that if internal knots are not repeated, the B-Spline basis functions are at least C^{p-1}-continuous everywhere. More specifically, if a knot has multiplicity $\hbar$, the basis is $C^{p-\hbar}$-continuous at that knot. In Fig. 1 we present an example of quadratic B-spline basis functions generated from the uniform open knot vector $\Xi = \{0, 0, 0, 1, 2, 3, 4, 5, 6, 6, 6\}$.

NURBS are built from B-splines. In particular, a NURBS entity in $\mathbb{R}^d$ can be obtained by a projective transformation of a B-spline object in $\mathbb{R}^{d+1}$. Given the B-spline basis function $N_{i,p}(\xi)$, the one dimensional NURBS basis can be defined as

$$\mathcal{R}_i^p(\xi) = \frac{N_{i,p}(\xi)\, w_i}{\sum_{\hat{i}=1}^{n_c} N_{i,p}(\xi)\, w_{\hat{i}}}, \tag{3}$$

where w_i is a positive real weight. For the two and three dimensional cases, the NURBS basis functions are given by

$$\mathcal{R}_{i,j}^{p,q}(\xi,\eta) = \frac{N_{i,p}(\xi)\, M_{j,q}(\eta)\, w_{i,j}}{\sum_{\hat{i}=1}^{n_c}\sum_{\hat{j}=1}^{m_c} N_{\hat{i},p}(\xi)\, M_{\hat{j},q}(\eta)\, w_{\hat{i},\hat{j}}}, \tag{4}$$

$$\mathcal{R}_{i,j,k}^{p,q,\imath}(\xi,\eta,\zeta) = \frac{N_{i,p}(\xi)\, M_{j,q}(\eta)\, L_{k,\imath}(\zeta)\, w_{i,j,k}}{\sum_{\hat{i}=1}^{n_c}\sum_{\hat{j}=1}^{m_c}\sum_{\hat{k}=1}^{l_c} N_{i,p}(\xi)\, M_{\hat{j},q}(\eta)\, L_{\hat{k},\imath}(\zeta)\, w_{\hat{i},\hat{j},\hat{k}}}. \tag{5}$$

In the expressions above, $\Xi = \{\xi_1, ..., \xi_{n_c+p+1}\}$, $\mathcal{H} = \{\eta_1, ..., \eta_{m_c+q+1}\}$ and $\mathcal{Z} = \{\zeta_1, ..., \zeta_{l_c+\imath+1}\}$ are the knot vectors; p, q and $\imath$ denote the polynomial orders, and $w_{\hat{i},\hat{j}}$ and $w_{\hat{i},\hat{j},\hat{k}}$ are the weights. Note that the NURBS basis functions are no longer piecewise polynomials, but piecewise rationals. They can exactly represent all conic sections. NURBS functions inherit most of the properties of B-splines. They are pointwise nonnegative and they still constitute a partition of unity. Their continuity, as well as their support is the same as for B-splines. Note also that if the weights are all equal, as it is the case for the computations presented herein, then NURBS basis functions reduce to B-splines basis functions, i.e, $\mathcal{R}_i^p(\xi) = N_{i,p}(\xi)$.

Given a mesh of control points, $\{\boldsymbol{B}_i\}$, $i = 1, 2, ..., n_c$, polynomial order p and knot vector $\Xi = \{\xi_1, ..., \xi_{n_c+p+1}\}$ a NURBS curve may be defined as

$$\boldsymbol{C}(\xi) = \sum_{i=1}^{n_c} \mathcal{R}_i^p(\xi)\, \boldsymbol{B}_i. \tag{6}$$

Analogously, a NURBS surface $\boldsymbol{S}(\xi,\eta)$ and a NURBS volume $\boldsymbol{V}(\xi,\eta,\zeta)$ may be defined as

$$\boldsymbol{S}(\xi,\eta) = \sum_{i=1}^{n_c}\sum_{j=1}^{m_c} \mathcal{R}_{i,j}^{p,q}(\xi,\eta)\,\boldsymbol{B}_{i,j}, \tag{7}$$

$$\boldsymbol{V}(\xi,\eta,\zeta) = \sum_{i=1}^{n_c}\sum_{j=1}^{m_c}\sum_{k=1}^{l_c} \mathcal{R}_{i,j,k}^{p,q,\text{ż}}(\xi,\eta,\zeta)\,\boldsymbol{B}_{i,j,k}, \tag{8}$$

where $\{\boldsymbol{B}_{i,j}\}$ and $\{\boldsymbol{B}_{i,j,k}\}$ are the control points, $i = 1,2,...,n_c$, $j = 1,2,...,m_c$, $k = 1,2,...,l_c$.

IGA is compatible with the two classical mesh refinement strategies, knot insertion (h-refinement) and order elevation (p-refinement). However, there is a third option, referred to as k-refinement (see, e.g., [64]), which allows to increase the order and the smoothness of the NURBS basis functions simultaneously. As in finite elements, in Isogeometric Analysis the isoparametric concept is used, which means that the unknown variables are represented in terms of the same NURBS functions [see Eqs. (3)-(5)] that are used for defining the geometry.

Remark

In what follows, for simplicity, we will omit the index of the basis functions that represents the polynomial degree. This information will be inferred from the context.

3. Mathematical model

In this section, we show how our model can be derived from a free energy functional. By using a Coleman-Noll procedure [78] we will find sufficient conditions that must be satisfied to enforce the dissipation inequality for any arbitrary solution of the theory. We will also show that our model fulfills those conditions. For simplicity, we will focus on the isothermal case, but similar arguments may be used to derive a thermally-coupled theory (see, e.g., [63]).

3.1. Energy functional

Let us define the total energy of the system

$$\mathcal{E}(\rho,\boldsymbol{u}) = \int_\Omega \left(\Psi + \frac{1}{2}\rho\,|\boldsymbol{u}|^2\right) \mathrm{d}\Omega, \tag{9}$$

where Ω is an open subset of $\mathbb{R}^3$ and $|\cdot|$ denotes the Euclidean norm of a vector; ρ is the fluid density and $\boldsymbol{u}$ represents the velocity vector. The free energy Ψ is assumed to belong to the following constitutive class

$$\Psi = \widehat{\Psi}(\boldsymbol{L},\rho,\nabla\rho,c)\,. \tag{10}$$

In the above expression, c is the surfactant concentration and $\boldsymbol{L}$ is the symmetric part of the velocity gradient, that is,

$$\boldsymbol{L} = \frac{1}{2}\left(\nabla\boldsymbol{u} + \nabla\boldsymbol{u}^T\right), \tag{11}$$

where $\square^T$ denotes the transpose of $\square$.

3.2. Derivation of the model

Our starting point will be the classical balance laws for mass of fluid and surfactant [see Eqs. (12) and (15), respectively], linear momentum [Eq. (13)] and angular momentum [Eq. (14)]. These equations may be written as,

$$\dot{\rho} + \rho\nabla\cdot\boldsymbol{u} = 0, \tag{12}$$

$$\rho\dot{\boldsymbol{u}} = \nabla\cdot\boldsymbol{T} + \rho\boldsymbol{f}, \tag{13}$$

$$\boldsymbol{T} = \boldsymbol{T}^T, \tag{14}$$

$$\dot{c} + c\nabla\cdot\boldsymbol{u} = -\nabla\cdot\boldsymbol{j}, \tag{15}$$

where $\boldsymbol{T}$ is the Cauchy stress tensor, $\boldsymbol{f}$ represents body forces per unit mass and $\boldsymbol{j}$ describes the mass flux of surfactant; $\dot{\square}$ denotes the material time derivative of $\square$ and may also be expressed as $\partial\square/\partial t + \boldsymbol{u}\cdot\nabla\square$. The quantity $\dot{\square}$ may also be understood as the time derivative of $\square$ holding the material particle fixed.

Our goal is to find a constitutive equation for $\boldsymbol{T}$ and $\boldsymbol{j}$ so that the energy of the system decreases with time for any arbitrary solution of the theory. In order to do so, we will use the framework of thermomechanics and the Coleman-Noll approach. We will assume that $\boldsymbol{T}$ belongs to the constitutive class

$$\boldsymbol{T} = \widehat{\boldsymbol{T}}\left(\boldsymbol{L}, \rho, \nabla\rho, c, \mu\right), \tag{16}$$

where μ is the chemical potential and is defined as

$$\mu = \frac{\delta}{\delta\rho}\left(\int_\Omega \Psi \mathrm{d}\Omega\right) = \frac{\partial\widehat{\Psi}}{\partial\rho} - \nabla\cdot\left(\frac{\partial\widehat{\Psi}}{\partial\nabla\rho}\right), \tag{17}$$

with $\dfrac{\delta}{\delta\rho}$ denoting the variational derivative with respect to density. Let us also define the following energy dissipation law

$$\mathcal{R} = \frac{\mathrm{d}}{\mathrm{d}t}\left\{\int_{\mathscr{P}_t}\left(\Psi + \frac{1}{2}\rho\left|\boldsymbol{u}\right|^2\right)\mathrm{d}\mathscr{P}_t\right\} = \mathscr{W}\left(\mathscr{P}_t\right) - \mathscr{D}\left(\mathscr{P}_t\right) + \Phi\left(\partial\mathscr{P}_t\right) \qquad \text{with} \qquad \mathscr{D}\left(\mathscr{P}_t\right) \geq 0. \tag{18}$$

Here, $\mathscr{P}_t$ is an arbitrary set of material particles and $\partial\mathscr{P}_t$ denotes its boundary. $\mathscr{W}\left(\mathscr{P}_t\right)$ is the work associated to the external forces, $\Phi\left(\partial\mathscr{P}_t\right)$ represents the energy supplies coming through $\partial\mathscr{P}_t$ and $\mathscr{D}\left(\mathscr{P}_t\right)$ is the dissipation, which must be non-negative for all conceivable processes. Using the Reynolds transport theorem (see, for example, [83]), it follows that

$$\frac{\mathrm{d}}{\mathrm{d}t}\left\{\int_{\mathscr{P}_t}\Psi\mathrm{d}\mathscr{P}_t\right\} = \int_{\mathscr{P}_t}\left(\dot{\Psi} + \Psi\nabla\cdot\boldsymbol{u}\right)\mathrm{d}\mathscr{P}_t, \tag{19}$$

$$\begin{aligned}\frac{\mathrm{d}}{\mathrm{d}t}\left\{\int_{\mathscr{P}_t}\frac{1}{2}\rho\left|\boldsymbol{u}\right|^2\mathrm{d}\mathscr{P}_t\right\} &= \int_{\mathscr{P}_t}\left[\left(\frac{1}{2}\rho\left|\boldsymbol{u}\right|^2\right)^{\cdot} + \frac{1}{2}\rho\left|\boldsymbol{u}\right|^2\nabla\cdot\boldsymbol{u}\right]\mathrm{d}\mathscr{P}_t = \int_{\mathscr{P}_t}\left(\frac{1}{2}\dot{\rho}\left|\boldsymbol{u}\right|^2 + \rho\boldsymbol{u}\cdot\dot{\boldsymbol{u}} + \frac{1}{2}\rho\left|\boldsymbol{u}\right|^2\nabla\cdot\boldsymbol{u}\right)\mathrm{d}\mathscr{P}_t \\ &= \int_{\mathscr{P}_t}\rho\boldsymbol{u}\cdot\dot{\boldsymbol{u}}\mathrm{d}\mathscr{P}_t.\end{aligned} \tag{20}$$

Note that in (20) we have used the mass conservation equation (12). Taking into account the constitutive class of Ψ given by Eq. (10), and relations (19) and (20), the dissipation law can be written

$$\mathcal{R} = \frac{\mathrm{d}}{\mathrm{d}t}\left\{\int_{\mathscr{P}_t}\left(\Psi + \frac{1}{2}\rho\left|\boldsymbol{u}\right|^2\right)\mathrm{d}\mathscr{P}_t\right\} = \int_{\mathscr{P}_t}\left(\frac{\partial\widehat{\Psi}}{\partial\boldsymbol{L}} : \dot{\boldsymbol{L}} + \frac{\partial\widehat{\Psi}}{\partial\rho}\dot{\rho} + \frac{\partial\widehat{\Psi}}{\partial\nabla\rho}\cdot(\nabla\rho)^{\cdot} + \frac{\partial\widehat{\Psi}}{\partial c}\dot{c} + \Psi\nabla\cdot\boldsymbol{u} + \rho\boldsymbol{u}\cdot\dot{\boldsymbol{u}}\right)\mathrm{d}\mathscr{P}_t, \tag{21}$$

where the symbol : denotes the usual double-dot product. At this point, we introduce the classical relation

$$(\nabla\rho)^{\cdot} = \nabla\dot{\rho} - \nabla\boldsymbol{u}\nabla\rho, \tag{22}$$

In component notation, the vector $\nabla\boldsymbol{u}\nabla\rho$ would be understood as the product of a square matrix ($\nabla\boldsymbol{u}$) with a column vector ($\nabla\rho$), that is, $[\nabla\boldsymbol{u}\nabla\rho]_i = \frac{\partial u_i}{\partial x_j}\frac{\partial\rho}{\partial x_j}$. Using Eqs. (13), (15) and (22), $\mathcal{R}$ results in the following expression

$$\mathcal{R} = \int_{\mathscr{P}_t}\left(\frac{\partial\widehat{\Psi}}{\partial\boldsymbol{L}} : \dot{\boldsymbol{L}} + \frac{\partial\widehat{\Psi}}{\partial\rho}\dot{\rho} + \frac{\partial\widehat{\Psi}}{\partial\nabla\rho}\cdot\nabla\dot{\rho} - \frac{\partial\widehat{\Psi}}{\partial\nabla\rho}\cdot\nabla\boldsymbol{u}\nabla\rho - \frac{\partial\widehat{\Psi}}{\partial c}\nabla\cdot\boldsymbol{j} - \frac{\partial\widehat{\Psi}}{\partial c}c\nabla\cdot\boldsymbol{u} + \Psi\nabla\cdot\boldsymbol{u} + \boldsymbol{u}\cdot(\nabla\cdot\boldsymbol{T} + \rho\boldsymbol{f})\right)\mathrm{d}\mathscr{P}_t. \tag{23}$$

Integrating by parts the terms with $\nabla\dot{\rho}$, $\nabla\cdot\boldsymbol{j}$ and $\nabla\cdot\boldsymbol{T}$, we obtain

$$\begin{aligned}\mathcal{R} = &\int_{\mathscr{P}_t}\left(\frac{\partial\widehat{\Psi}}{\partial\boldsymbol{L}} : \dot{\boldsymbol{L}} + \frac{\partial\widehat{\Psi}}{\partial\rho}\dot{\rho} - \nabla\cdot\left(\frac{\partial\widehat{\Psi}}{\partial\nabla\rho}\right)\dot{\rho} - \frac{\partial\widehat{\Psi}}{\partial\nabla\rho}\cdot\nabla\boldsymbol{u}\nabla\rho + \nabla\left(\frac{\partial\widehat{\Psi}}{\partial c}\right)\cdot\boldsymbol{j} - \frac{\partial\widehat{\Psi}}{\partial c}c\nabla\cdot\boldsymbol{u} + \Psi\nabla\cdot\boldsymbol{u} - \boldsymbol{T} : \nabla\boldsymbol{u} + \rho\boldsymbol{u}\cdot\boldsymbol{f}\right)\mathrm{d}\mathscr{P}_t \\ &+ \int_{\partial\mathscr{P}_t}\left(\dot{\rho}\frac{\partial\widehat{\Psi}}{\partial\nabla\rho}\cdot\boldsymbol{n} - \frac{\partial\widehat{\Psi}}{\partial c}\boldsymbol{j}\cdot\boldsymbol{n} + \boldsymbol{u}\cdot\boldsymbol{T}\boldsymbol{n}\right)\mathrm{d}(\partial\mathscr{P}_t).\end{aligned} \tag{24}$$

Let us now use that

$$\frac{\partial\widehat{\Psi}}{\partial\nabla\rho}\cdot\nabla\boldsymbol{u}\nabla\rho=\frac{\partial\widehat{\Psi}}{\partial\nabla\rho}\otimes\nabla\rho:\nabla\boldsymbol{u}, \tag{25}$$

$$\nabla\cdot\boldsymbol{u}=\boldsymbol{I}:\nabla\boldsymbol{u}, \tag{26}$$

where $\boldsymbol{I}$ represents the identity tensor and $\otimes$ denotes the usual vector outer product. With these identities in mind and using the mass balance equation (12), it can be shown that $\mathcal{R}$ takes on the form

$$\begin{aligned}\mathcal{R}=&\int_{\mathscr{P}_t}\left(\frac{\partial\widehat{\Psi}}{\partial\boldsymbol{L}}:\dot{\boldsymbol{L}}-\frac{\partial\widehat{\Psi}}{\partial\rho}\rho\boldsymbol{I}:\nabla\boldsymbol{u}+\nabla\cdot\left(\frac{\partial\widehat{\Psi}}{\partial\nabla\rho}\right)\rho\boldsymbol{I}:\nabla\boldsymbol{u}-\frac{\partial\widehat{\Psi}}{\partial\nabla\rho}\otimes\nabla\rho:\nabla\boldsymbol{u}+\nabla\left(\frac{\partial\widehat{\Psi}}{\partial c}\right)\cdot\boldsymbol{j}\right)\mathrm{d}\mathscr{P}_t\\&+\int_{\mathscr{P}_t}\left(-\frac{\partial\widehat{\Psi}}{\partial c}c\boldsymbol{I}:\nabla\boldsymbol{u}+\Psi\boldsymbol{I}:\nabla\boldsymbol{u}-\boldsymbol{T}:\nabla\boldsymbol{u}+\rho\boldsymbol{u}\cdot\boldsymbol{f}\right)\mathrm{d}\mathscr{P}_t+\int_{\partial\mathscr{P}_t}\left(\dot{\rho}\frac{\partial\widehat{\Psi}}{\partial\nabla\rho}\cdot\boldsymbol{n}-\frac{\partial\widehat{\Psi}}{\partial c}\boldsymbol{j}\cdot\boldsymbol{n}+\boldsymbol{u}\cdot\boldsymbol{T}\boldsymbol{n}\right)\mathrm{d}(\partial\mathscr{P}_t)\\=&\int_{\mathscr{P}_t}\left(\frac{\partial\widehat{\Psi}}{\partial\boldsymbol{L}}:\dot{\boldsymbol{L}}+\left[\left(-\frac{\partial\widehat{\Psi}}{\partial\rho}\rho+\nabla\cdot\left(\frac{\partial\widehat{\Psi}}{\partial\nabla\rho}\right)\rho-\frac{\partial\widehat{\Psi}}{\partial c}c+\Psi\right)\boldsymbol{I}-\boldsymbol{T}-\frac{\partial\widehat{\Psi}}{\partial\nabla\rho}\otimes\nabla\rho\right]:\nabla\boldsymbol{u}+\nabla\left(\frac{\partial\widehat{\Psi}}{\partial c}\right)\cdot\boldsymbol{j}+\rho\boldsymbol{u}\cdot\boldsymbol{f}\right)\mathrm{d}\mathscr{P}_t\\&+\int_{\partial\mathscr{P}_t}\left(\dot{\rho}\frac{\partial\widehat{\Psi}}{\partial\nabla\rho}\cdot\boldsymbol{n}-\frac{\partial\widehat{\Psi}}{\partial c}\boldsymbol{j}\cdot\boldsymbol{n}+\boldsymbol{u}\cdot\boldsymbol{T}\boldsymbol{n}\right)\mathrm{d}(\partial\mathscr{P}_t)\end{aligned} \tag{27}$$

Examining the previous expression and comparing it with the energy dissipation law defined in Eq. (18), we can identify the working $\mathscr{W}(\mathscr{P}_t)$, the dissipation $\mathscr{D}(\mathscr{P}_t)$ and the energy supplies across the boundaries $\Phi(\partial\mathscr{P}_t)$ as

$$\Phi(\partial\mathscr{P}_t)=\int_{\partial\mathscr{P}_t}\left(\dot{\rho}\frac{\partial\widehat{\Psi}}{\partial\nabla\rho}\cdot\boldsymbol{n}-\frac{\partial\widehat{\Psi}}{\partial c}\boldsymbol{j}\cdot\boldsymbol{n}+\boldsymbol{u}\cdot\boldsymbol{T}\boldsymbol{n}\right)\mathrm{d}(\partial\mathscr{P}_t), \tag{28}$$

$$\mathscr{D}(\mathscr{P}_t)=\int_{\mathscr{P}_t}\left(-\frac{\partial\widehat{\Psi}}{\partial\boldsymbol{L}}:\dot{\boldsymbol{L}}+\left[\left(\mu\rho-\Psi+\frac{\partial\widehat{\Psi}}{\partial c}c\right)\boldsymbol{I}+\boldsymbol{T}+\frac{\partial\widehat{\Psi}}{\partial\nabla\rho}\otimes\nabla\rho\right]:\nabla\boldsymbol{u}-\nabla\left(\frac{\partial\widehat{\Psi}}{\partial c}\right)\cdot\boldsymbol{j}\right)\mathrm{d}\mathscr{P}_t, \tag{29}$$

$$\mathscr{W}(\mathscr{P}_t)=\int_{\mathscr{P}_t}\rho\boldsymbol{u}\cdot\boldsymbol{f}\mathrm{d}\mathscr{P}_t. \tag{30}$$

Note that in Eq. (29) we have used the definition of μ given in (17). At this point we just need to find constitutive equations for $\boldsymbol{T}$ and $\boldsymbol{j}$ such that $\mathcal{E}$ decreases with time for any arbitrary solution of the theory. This can be guaranteed by imposing $\mathscr{D}(\mathscr{P}_t)\geq 0$ for all conceivable processes. In order to do so, we will analyze all the terms in expression (29). For the first term, we will take into account that the constitutive class of Ψ [see Eq. (10)] does not allow the dependence of Ψ on $\dot{\boldsymbol{L}}$. Therefore, the only way to ensure that this term is pointwisely positive or zero is by taking

$$\frac{\partial\widehat{\Psi}}{\partial\boldsymbol{L}}=0. \tag{31}$$

Focusing now on the last term of Eq. (29), the constitutive choice

$$\boldsymbol{j}=-\kappa\nabla\left(\frac{\partial\widehat{\Psi}}{\partial c}\right)\qquad\text{with}\qquad\kappa>0, \tag{32}$$

guarantees that this term will be pointwise non-negative. Considering this, we enforce the inequality

$$\left[\left(\mu\rho-\Psi+c\frac{\partial\widehat{\Psi}}{\partial c}\right)\boldsymbol{I}+\boldsymbol{T}+\frac{\partial\widehat{\Psi}}{\partial\nabla\rho}\otimes\nabla\rho\right]:\nabla\boldsymbol{u}\geq 0. \tag{33}$$

Note that Eqs. (31)–(33) are sufficient conditions to guarantee $\mathscr{D}(\mathscr{P}_t)\geq 0$. To obtain a constitutive equation for $\boldsymbol{T}$ that verifies Eq. (33) we assume, without loss of generality, the following splitting of the velocity gradient

$$\nabla\boldsymbol{u}=\boldsymbol{L}+\boldsymbol{W}=\boldsymbol{L}^d+\boldsymbol{L}^h+\boldsymbol{W}, \tag{34}$$

where $\boldsymbol{W}$ is the skew-symmetric part of the velocity gradient

$$\boldsymbol{W} = \frac{1}{2}\left(\nabla \boldsymbol{u} - \nabla \boldsymbol{u}^T\right), \tag{35}$$

and $\boldsymbol{L}^h$ and $\boldsymbol{L}^d$ are the dilatational and the deviatoric parts of $\boldsymbol{L}$, that is,

$$\boldsymbol{L}^h = \frac{1}{3}\nabla \cdot \boldsymbol{u}\boldsymbol{I}, \tag{36}$$

$$\boldsymbol{L}^d = \boldsymbol{L} - \frac{1}{3}\nabla \cdot \boldsymbol{u}\boldsymbol{I}. \tag{37}$$

It is easily seen that both $\boldsymbol{L}^d$ and $\boldsymbol{L}^h$ are symmetric tensors and that $\boldsymbol{L}^d$ is traceless, i.e., $\mathrm{tr}(\boldsymbol{L}^d) = 0$. Using now Eqs. (34), (35) and (14), it is straightforward to obtain the following identities

$$\boldsymbol{T} : \nabla \boldsymbol{u} = \boldsymbol{T} : (\boldsymbol{L} + \boldsymbol{W}) = \boldsymbol{T} : \boldsymbol{L}, \tag{38}$$

$$\boldsymbol{I} : \nabla \boldsymbol{u} = \boldsymbol{I} : (\boldsymbol{L} + \boldsymbol{W}) = \boldsymbol{I} : \boldsymbol{L}. \tag{39}$$

Additionally, frame invariance arguments may be used (see, e.g., [84]) to show that $\dfrac{\partial \widehat{\Psi}}{\partial \nabla \rho} \otimes \nabla \rho$ is a symmetric tensor. Therefore,

$$\frac{\partial \widehat{\Psi}}{\partial \nabla \rho} \otimes \nabla \rho : \nabla \boldsymbol{u} = \frac{\partial \widehat{\Psi}}{\partial \nabla \rho} \otimes \nabla \rho : \boldsymbol{L}. \tag{40}$$

Taking into account Eqs. (38), (39) and (40), we can rewrite the inequality (33) as

$$\left[\left(\mu\rho - \Psi + c\frac{\partial \widehat{\Psi}}{\partial c}\right)\boldsymbol{I} + \boldsymbol{T} + \frac{\partial \widehat{\Psi}}{\partial \nabla \rho} \otimes \nabla \rho\right] : \boldsymbol{L} \geq 0. \tag{41}$$

The goal now is to choose the term in brackets in (41) in such a way that its double contraction with $\boldsymbol{L}$ is non-negative. We will prove that this can be achieved taking

$$\left[\mu\rho - \Psi + c\frac{\partial \widehat{\Psi}}{\partial c}\right]\boldsymbol{I} + \boldsymbol{T} + \frac{\partial \widehat{\Psi}}{\partial \nabla \rho} \otimes \nabla \rho = 2\bar{\mu}\boldsymbol{L} + \bar{\lambda}\nabla \cdot \boldsymbol{u}\boldsymbol{I}, \tag{42}$$

where $\bar{\mu}$ and $\bar{\lambda}$ are viscosity coefficients that must fulfill a series of conditions that will be shown later. Using Eqs. (36), (37) and basic properties of the double dot product, we obtain

$$\begin{aligned}
\left(2\bar{\mu}\boldsymbol{L} + \bar{\lambda}\nabla \cdot \boldsymbol{u}\boldsymbol{I}\right) : \boldsymbol{L} &= 2\bar{\mu}\boldsymbol{L} : \boldsymbol{L} + \bar{\lambda}\nabla \cdot \boldsymbol{u}\,(\boldsymbol{I} : \boldsymbol{L}) \\
&= 2\bar{\mu}\boldsymbol{L}^d : \boldsymbol{L}^d + 4\bar{\mu}\boldsymbol{L}^d : \boldsymbol{L}^h + 2\bar{\mu}\boldsymbol{L}^h : \boldsymbol{L}^h + \bar{\lambda}\nabla \cdot \boldsymbol{u}\,\mathrm{tr}\,(\boldsymbol{L}) \\
&= 2\bar{\mu}\mathrm{tr}\left((\boldsymbol{L}^d)^2\right) + \frac{4}{3}\bar{\mu}\nabla \cdot \boldsymbol{u}\,\mathrm{tr}(\boldsymbol{L}^d) + \frac{2}{9}\bar{\mu}\,(\nabla \cdot \boldsymbol{u})^2\,\mathrm{tr}\,(\boldsymbol{I}) + \bar{\lambda}\,(\nabla \cdot \boldsymbol{u})^2 \\
&= 2\bar{\mu}\mathrm{tr}\left((\boldsymbol{L}^d)^2\right) + \left(\frac{2}{3}\bar{\mu} + \bar{\lambda}\right)(\nabla \cdot \boldsymbol{u})^2\,.
\end{aligned} \tag{43}$$

Therefore, since $\mathrm{tr}\left((\boldsymbol{L}^d)^2\right) = \sum_{ij}(L^d_{ij})^2 \geq 0$, it follows that

$$\left(2\bar{\mu}\boldsymbol{L} + \bar{\lambda}\nabla \cdot \boldsymbol{u}\boldsymbol{I}\right) : \boldsymbol{L} \geq 0 \tag{44}$$

for any $\bar{\mu}$ and $\bar{\lambda}$ such that,

$$\frac{2}{3}\bar{\mu} + \bar{\lambda} \geq 0 \qquad \text{and} \qquad \bar{\mu} \geq 0. \tag{45}$$

Note that our choice in Eq. (42) leads to a classical model of Newtonian fluids if we assume that $\widehat{\Psi}$ depends neither on $\nabla\rho$ nor on c.

To complete the theory, we need to define the nonlinear function Ψ. Within the constitutive class given by Eq. (10), we consider the expression

$$\widehat{\Psi}(\rho, \nabla\rho, c) = \mathcal{W}(\rho) + \frac{\lambda(c)}{2}|\nabla\rho|^2 + \mathcal{U}(c), \tag{46}$$

where λ is a function of c that takes positive values and $\mathcal{U}(c)$ is the free energy associated to the surfactant. The second term represents the free energy that leads to the capillary forces at the gas-liquid interfaces. $\mathcal{W}(\rho)$ is the Helmholtz free energy of a van der Waals fluid [61, 85], which is given by

$$\mathcal{W}(\rho) = R\theta\rho\log\left(\frac{\rho}{b-\rho}\right) - a\rho^2. \tag{47}$$

In the above expression, a and b are positive constants, R is the specific gas constant and θ represents the temperature of the system. Eq. (47) may be thought of as a higher-order modification of the perfect gas Helmholtz free energy that allows for spontaneous phase changes. The ability of Eq. (47) to predict phase transformations stems from the fact that $\mathcal{W}$ may be a non-convex function of ρ for low temperatures. Using Eq. (46) and isolating the stress tensor in (42), we obtain the following expression for $\boldsymbol{T}$

$$\begin{aligned}\boldsymbol{T} = &\left[\mathcal{W}(\rho) + \frac{\lambda(c)}{2}|\nabla\rho|^2 + \mathcal{U}(c) - \rho\mathcal{W}'(\rho) + \rho\lambda'(c)\nabla c\cdot\nabla\rho + \lambda(c)\rho\Delta\rho - c\frac{\lambda'(c)}{2}|\nabla\rho|^2 - c\ \ \mathcal{U}'(c)\right]\boldsymbol{I}\\ &- \lambda(c)\nabla\rho\otimes\nabla\rho + 2\bar{\mu}\boldsymbol{L} + \bar{\lambda}\nabla\cdot\boldsymbol{u}\boldsymbol{I}.\end{aligned} \tag{48}$$

Finally, identifying $\rho\mathcal{W}'(\rho) - \mathcal{W}(\rho)$ with the thermodynamic pressure p, the stress tensor $\boldsymbol{T}$ can be written as

$$\begin{aligned}\boldsymbol{T} = &-p\boldsymbol{I} + \left[\frac{1}{2}(\lambda(c) - c\lambda'(c))|\nabla\rho|^2 + \mathcal{U}(c) - c\ \ \mathcal{U}'(c) + \rho\lambda'(c)\nabla c\cdot\nabla\rho + \lambda(c)\rho\Delta\rho\right]\boldsymbol{I}\\ &- \lambda(c)\nabla\rho\otimes\nabla\rho + 2\bar{\mu}\boldsymbol{L} + \bar{\lambda}\nabla\cdot\boldsymbol{u}\boldsymbol{I}.\end{aligned} \tag{49}$$

For the surfactant energy $\mathcal{U}(c)$, there are several possible choices. One of the simplest options is to consider $\mathcal{U}(c) = c^2\alpha/2$ where α is a positive constant. This is the free energy associated to classical diffusion processes. With this expression in mind, the stress tensor becomes

$$\boldsymbol{T} = -p\boldsymbol{I} + \left[\frac{1}{2}(\lambda(c) - c\lambda'(c))|\nabla\rho|^2 - \frac{\alpha}{2}c^2 + \rho\lambda'(c)\nabla c\cdot\nabla\rho + \lambda(c)\rho\Delta\rho\right]\boldsymbol{I} - \lambda(c)\nabla\rho\otimes\nabla\rho + 2\bar{\mu}\boldsymbol{L} + \bar{\lambda}\nabla\cdot\boldsymbol{u}\boldsymbol{I}. \tag{50}$$

Note also that the stress tensor is symmetric, ensuring that the angular momentum equation (14) is satisfied. This completes the derivation of the theory.

4. Numerical algorithm

4.1. Governing equations

We start by recasting the governing equations in a convenient form for our numerical algorithms. Using the definition of the material time derivative, and the fundamental equations defined in (12), (13) and (15), it is straightforward to obtain the Navier-Stokes-Korteweg equations with surfactant in the Eulerian description as follows

$$\frac{\partial\rho}{\partial t} + \nabla\cdot(\rho\boldsymbol{u}) = 0, \tag{51}$$

$$\frac{\partial(\rho\boldsymbol{u})}{\partial t} + \nabla\cdot(\rho\boldsymbol{u}\otimes\boldsymbol{u}) - \nabla\cdot\boldsymbol{T} - \rho\boldsymbol{f} = 0, \tag{52}$$

$$\frac{\partial c}{\partial t} + \nabla\cdot(c\boldsymbol{u}) + \nabla\cdot\boldsymbol{j} = 0. \tag{53}$$

Notice that the rest of the elements that completely define the theory, that is, a constitutive equation for the stress tensor and the surfactant mass flux as well as a thermodynamic potential from which we can derive the state variables, have already been defined in Section 3.2. Nevertheless, these elements will be analyzed in more detail in the following sections.

4.1.1. Stress tensor

The constitutive equation for the stress tensor $\boldsymbol{T}$ was defined in (50). However, in order to simplify the notation we will adopt the following splitting

$$\boldsymbol{T} = \boldsymbol{\tau} - p\boldsymbol{I} + \boldsymbol{\varsigma} + \boldsymbol{\varsigma}_s, \tag{54}$$

where

$$\boldsymbol{\tau} = \bar{\mu}\left(\nabla\boldsymbol{u} + \nabla\boldsymbol{u}^T\right) + \bar{\lambda}\nabla\cdot\boldsymbol{u}\boldsymbol{I}, \tag{55}$$

$$\boldsymbol{\varsigma} = \lambda(c)\left(\rho\Delta\rho + \frac{1}{2}|\nabla\rho|^2\right)\boldsymbol{I} - \lambda(c)\nabla\rho\otimes\nabla\rho, \tag{56}$$

$$\boldsymbol{\varsigma}_s = \left(-\frac{\alpha}{2}c^2 - c\frac{\lambda'(c)}{2}|\nabla\rho|^2 + \rho\lambda'(c)\nabla c\cdot\nabla\rho\right)\boldsymbol{I}. \tag{57}$$

In the above expressions, $\boldsymbol{\varsigma}$ is the so-called Korteweg tensor, $\boldsymbol{\varsigma}_s$ is the part of the stress tensor associated to the surfactant and $\boldsymbol{\tau}$ corresponds to the viscous stress tensor of a Newtonian fluid (see, for example, [86]). Throughout this paper, we will assume that the Stokes hypothesis is satisfied, that is, $\bar{\lambda} = -2\bar{\mu}/3$. Finally, λ is a function that takes positive values and that modulates the strength of capillary forces. Later, we will show that λ is related with the surface tension at liquid-vapor interfaces. In particular, surface tension scales approximately linearly with $\sqrt{\lambda}$. Our goal is to model the capability of surfactants to lower surface tension. For this reason, λ must be a decreasing function of the surfactant concentration c. There are several possible choices for $\lambda(c)$. Among them, we adopt the following expression

$$\lambda(c) = \lambda_{min}g(c), \tag{58}$$

where λ_{min} is a positive constant that represents the minimum value allowed for the capillarity coefficient. Later, we will adopt a value for λ_{min} that depends on the mesh size as proposed in [45]. The function g is defined as $g(c) = 1 + \beta e^{-c^2}$ where β is a positive constant that controls the strength with which the surface tension decreases with the surfactant concentration. Throughout this paper, we will use the value $\beta = 4$. Larger values of β would produce greater variations of the surface tension, and thus, a more significant impact of the surfactant on the dynamics. Lower values of β would reduce the influence of the surfactant distribution and would produce dynamics which are closer to those of a classical Navier-Stokes-Korteweg fluid. The detailed dependency of the solution on β and on the functional form of λ is an interesting topic that warrants further research.

Remarks

1. We wish to highlight the difference between λ and $\bar{\lambda}$. The former is a function that represents the strength of capillary forces while the latter is one of the viscosity coefficients.
2. Note that since $\boldsymbol{\varsigma}$ depends upon $\Delta\rho$, the linear momentum balance equation includes third-order partial differential operators.

4.1.2. Surfactant mass flux

The constitutive form of the mass flux $\boldsymbol{j}$ has already been defined in Eq. (32). Using the expression adopted for Ψ [Eq. (46)] and considering the particular case in which $\mathcal{U}(c) = c^2\alpha/2$, $\boldsymbol{j}$ may be expressed as

$$\boldsymbol{j} = -\kappa\nabla\left(\alpha c + \frac{\lambda'(c)}{2}|\nabla\rho|^2\right) = -\kappa\alpha\nabla c - \frac{\kappa}{2}\left(\lambda''(c)\nabla c\,|\nabla\rho|^2 + 2\lambda'(c)\nabla\nabla\rho^T\nabla\rho\right). \tag{59}$$

Notice that the parameters κ and α govern the relative strength of convection and diffusion processes in the surfactant equation. They will also allow to control the intensity with which the surfactant is drawn by liquid-vapor interfaces. Note also that since $\boldsymbol{j}$ depends upon $\nabla\nabla\rho^T$, the convection-diffusion equation (53) includes third-order partial differential operators.

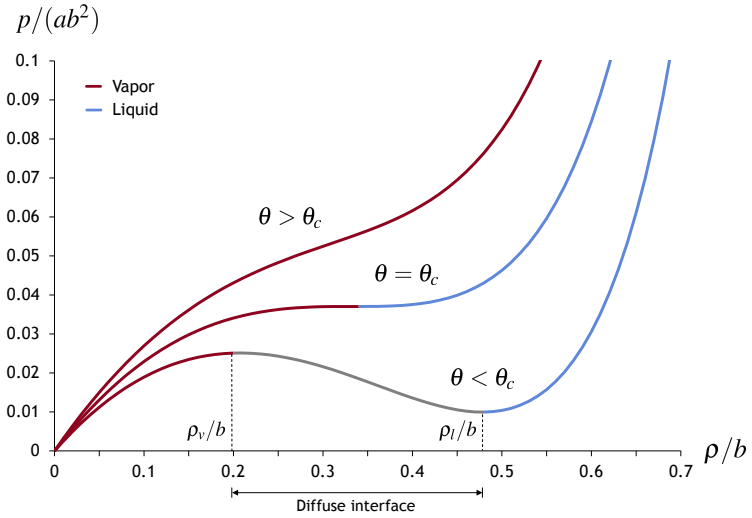

Figure 2: Non-dimensional plot of van der Waals pressure as a function of density for $\theta > \theta_c$, $\theta = \theta_c$ and $\theta < \theta_c$. Note that for values of temperature below the critical temperature ($\theta < \theta_c$), the pressure is a non-monotone function of density, which allows for spontaneous phase transformations.

4.1.3. State variables

In Section 3.2 we have seen that the thermodynamic pressure p can be identified as $\rho\mathcal{W}'(\rho) - \mathcal{W}(\rho)$. Using van der Waals-Helmholtz free energy (47), it is straightforward to obtain

$$p = Rb\left(\frac{\rho\theta}{b-\rho}\right) - a\rho^2. \tag{60}$$

The above equation is known as van der Waals equation and gives the pressure in terms of density and temperature, which for the isothermal model is assumed to be constant. Considering θ as a parameter, we can represent a non-dimensional plot of the pressure as a function of density for different values of θ (see Fig. 2). In this figure, we can observe different behaviors of the function p for temperatures below and above a critical temperature $\theta_c = 8ab/(27R)$. For $\theta > \theta_c$, p is a monotonically increasing function of ρ, and the only phase that is stable is the vapor phase. However, for values of the temperature below the critical temperature, that is, $\theta < \theta_c$, the pressure function is no longer monotone, and we can differentiate three regions. The density interval $\rho \in (0, \rho_v)$ corresponds to the vapor phase and the interval $\rho \in (\rho_l, b)$ corresponds to the liquid phase. Additionally, there exists a region $\rho \in (\rho_v, \rho_l)$ where the pressure function decreases with respect to density (grey line in Fig. 2). This allows for the fluid to evaporate and condensate naturally due to pressure and/or temperature variations without introducing additional fields and without precursors. The region where $\rho \in (\rho_v, \rho_l)$ has no physical meaning, however, mathematically it is just a smooth interface between the vapor and liquid phases which spans over a length scale $\sqrt{\lambda/a}$. Note also that in the inviscid, non-conducting limit, the equations are ill-posed for $\lambda = 0$, and capillary forces are necessary to restore well-posedness. The reader is referred to [45, 61, 85] for further details on the NSK equations without surfactants.

4.2. Boundary conditions

To define a well-posed boundary value problem we need to specify suitable boundary conditions. For some of the numerical examples that we will present in Section 5 we have adopted periodic boundary conditions. However, in order to analyze more practical situations we will consider other possibilities. In particular, we will focus on solid wall boundary conditions. In classical isothermal compressible gas dynamics, solid wall boundary conditions may be imposed, for example, by setting velocity to given values, that is, $\boldsymbol{u} = \boldsymbol{u}_D$ on the solid wall boundary. However, in the NSK system, the third-order spatial derivative on the density included in the linear momentum equation [see Eq. (56)] urges to impose an extra boundary condition to attain well-posedness. One possibility is to set the following boundary condition,

$$\nabla\rho \cdot \boldsymbol{n} = |\nabla\rho| \cos(\varphi), \tag{61}$$

where $\boldsymbol{n}$ denotes the unit outward normal to the boundary, and φ is the static contact angle between the liquid-vapor interface and the solid, measured in the liquid phase. To define suitable boundary conditions for the surfactant equation, we must take into account that surfactants are naturally trapped by liquid-vapor interfaces. Thus, the boundary conditions for the surfactant equation must be compatible with this phenomenon. For the majority of cases of practical relevance, we will also need the boundary conditions to be mass-preserving. With this idea in mind, we propose the following boundary condition,

$$\nabla c \cdot \boldsymbol{n} = |\nabla c| \cos(\varphi_s) \tag{62}$$

where φ_s represents the angle between the surfactant gradient and the outward normal to the boundary. We will relate φ_s with the contact angle φ in order to ensure that the surfactant is able to follow the liquid-vapor interface without any incompatibility caused by the presence of the boundary. To do so, we define the following relation,

$$\cos(\varphi_s) = \cos(\varphi) h(\rho) \tag{63}$$

with

$$h(\rho) = \tanh\left(\left(\frac{\rho_l^M + \rho_v^M}{2} - \rho\right) s\right) \tag{64}$$

In the above expression, s is a parameter that controls the slope of the hyperbolic tangent function and that we set to $s = 4/(\rho_l^M - \rho_v^M)$; the constants ρ_l^M and ρ_v^M denote the Maxwell states[2] for the liquid and the vapor phases, respectively. To define the function $h(\rho)$ in Eq. (64), let us first note that a typical equilibrium solution to our model produces a density profile which is composed by patches of constant density in which $\rho = \rho_l^M$ or $\rho = \rho_v^M$. These patches are linked by smooth transitions which span over a length scale $\sqrt{\lambda/a}$. Therefore, the function $h(\rho)$ produces a smooth and sufficiently fast transition between $+1$ and -1 when ρ varies in the interval $\rho \in \left(\rho_v^M, \rho_l^M\right)$. As a consequence, Eq. (64) enforces $\varphi_s \simeq \varphi$ for values of the density close to ρ_v^M and $\varphi_s \simeq \pi - \varphi$ for $\rho \simeq \rho_l^M$. The boundary condition (62)–(64) is also mass preserving. This is due to the fact that the surfactant gets quickly trapped on the liquid-vapor interface and $|\nabla c|$ is expected to be small everywhere else. Within the interface, there may be mass flow through the boundary, but the net contribution will be approximately zero because $h(\rho)$ is an odd function with respect to the contact line, which is assumed to be located at $\rho = (\rho_l^M + \rho_v^M)/2$.

4.3. Continuous problem in the weak form

Our derivation is based on a weak form of the governing equation. The usual practice to derive a weak form of a third-order partial differential equation is to introduce additional fields to lower the order of the derivatives in the variational form and use standard $\mathcal{C}^0$-continuous finite elements. Due to the use of IGA, we can generate globally $\mathcal{C}^1$-continuous basis functions and avoid the introduction of additional degrees of freedom. However, in order to facilitate the imposition of the boundary condition (61), we will introduce the new variable $\Upsilon = \Delta\rho$. The consequence of this choice is that our weak form will naturally enforce the boundary condition (61), which otherwise would have to be built strongly in the finite element space. As we will see later, our formulation still requires the use of $\mathcal{C}^1$-continuous basis functions and IGA due to the higher-order term in the surfactant equation.

We will consider that Eqs. (51)–(53) hold in $\Omega \subset \mathbb{R}^3$. The boundary of Ω is denoted Γ. To derive our weak form, let us introduce the trial solution space $\mathcal{X} = \mathcal{X}(\Omega)$. Let $\boldsymbol{U} = \{\rho, \boldsymbol{u}, \Upsilon, c\}$ be a typical member of $\mathcal{X}$. We assume that for all $\boldsymbol{U} \in \mathcal{X}$ the velocity field satisfies the solid-wall Dirichlet boundary condition on Γ. For the remaining fields in $\boldsymbol{U}$, namely ρ, Υ, and c, Dirichlet boundary conditions are not very relevant in practical applications, so we do not consider that case. The weighting function space $\mathcal{Y} = \mathcal{Y}(\Omega)$ is identical to $\mathcal{X}$, but all restrictions on the Dirichlet boundary are homogeneous. The variational formulation is stated as follows: Find $\boldsymbol{U} = \{\rho, \boldsymbol{u}, \Upsilon, c\} \in \mathcal{X}$ such that $\forall \boldsymbol{W} = \{w^1, \boldsymbol{w}^2, w^3, w^4\} \in \mathcal{Y}$,

$$B(\boldsymbol{W}, \boldsymbol{U}) = 0, \tag{65}$$

[2] The Maxwell states represent values of the density for which there is chemical and mechanical equilibrium. For a given temperature, they are simply the equilibrium values of the liquid and vapor densities.

where

$$
\begin{aligned}
B(\boldsymbol{W},\boldsymbol{U}) = &\int_\Omega w^1 \frac{\partial \rho}{\partial t}\mathrm{d}\Omega - \int_\Omega \nabla w^1 \cdot \boldsymbol{u}\rho \mathrm{d}\Omega + \int_\Omega \boldsymbol{w}^2 \cdot \left(\rho\frac{\partial \boldsymbol{u}}{\partial t} + \boldsymbol{u}\frac{\partial \rho}{\partial t} - \rho \boldsymbol{f}\right)\mathrm{d}\Omega - \int_\Omega \nabla \boldsymbol{w}^2 : \boldsymbol{u}\otimes\boldsymbol{u}\rho\mathrm{d}\Omega + \int_\Omega \nabla \boldsymbol{w}^2 : (\boldsymbol{\tau} - p\boldsymbol{I})\,\mathrm{d}\Omega \\
&+ \int_\Omega \nabla\cdot\boldsymbol{w}^2 \lambda(c)\left(\rho\Upsilon + \frac{1}{2}|\nabla\rho|^2\right)\mathrm{d}\Omega - \int_\Omega \nabla\boldsymbol{w}^2 : \lambda(c)\nabla\rho\otimes\nabla\rho\mathrm{d}\Omega - \int_\Omega \nabla\cdot\boldsymbol{w}^2\left(\frac{\alpha c^2}{2} + \frac{c\lambda'(c)}{2}|\nabla\rho|^2\right)\mathrm{d}\Omega \\
&+ \int_\Omega \nabla\cdot\boldsymbol{w}^2\lambda'(c)\rho\nabla c\cdot\nabla\rho\mathrm{d}\Omega + \int_\Omega w^3\Upsilon\mathrm{d}\Omega + \int_\Omega \nabla w^3\cdot\nabla\rho\mathrm{d}\Omega - \int_\Gamma w^3|\nabla\rho|\cos(\varphi)\mathrm{d}\Gamma + \int_\Omega w^4\frac{\partial c}{\partial t}\mathrm{d}\Omega \\
&- \int_\Omega \nabla w^4\cdot\boldsymbol{u}c\mathrm{d}\Omega + \int_\Omega \alpha\kappa\nabla w^4\cdot\nabla c\mathrm{d}\Omega - \int_\Gamma w^4\kappa\alpha|\nabla c|\cos(\varphi_s)\mathrm{d}\Gamma + \int_\Omega \frac{\kappa}{2}\nabla w^4\cdot\nabla\left(\lambda'(c)|\nabla\rho|^2\right)\mathrm{d}\Omega \\
&- \int_\Gamma w^4\frac{\kappa}{2}\lambda''(c)|\nabla\rho|^2|\nabla c|\cos(\varphi_s)\mathrm{d}\Gamma - \int_\Gamma w^4\kappa\lambda'(c)\nabla\nabla^T\rho\nabla\rho\cdot\boldsymbol{n}\mathrm{d}\Gamma
\end{aligned}
\tag{66}
$$

Note that the variational formulation (65)–(66) weakly imposes the fluid dynamics and the surfactant equations as well as the boundary conditions (61) and (62). Note also that if we do not set Dirichlet boundary conditions for velocity on the entire boundary, then the variational formulation weakly imposes the conjugate stress-free condition.

4.4. Semidiscrete formulation

For the spatial discretization of Eq. (66) we make use of the Galerkin method. We define finite-dimensional approximations of the functional spaces, namely, $\mathcal{X}_h$ and $\mathcal{Y}_h$, such that $\mathcal{X}_h \subset \mathcal{X} \subset \mathcal{H}^2$ and $\mathcal{Y}_h \subset \mathcal{Y} \subset \mathcal{H}^2$. Here, $\mathcal{H}^2$ denotes the Sobolev space of square integrable functions with square integrable first and second derivatives. We approximate (66) by the following variational problem over the finite element spaces: Find $\boldsymbol{U}_h = \{\rho_h, \boldsymbol{u}_h, \Upsilon_h, c_h\} \in \mathcal{X}_h$, such that $\forall \boldsymbol{W}_h = \{w_h^1, \boldsymbol{w}_h^2, w_h^3, w_h^4\} \in \mathcal{Y}_h$,

$$
B(\boldsymbol{W}_h, \boldsymbol{U}_h) = 0, \tag{67}
$$

where

$$
\rho_h(\boldsymbol{x},t) = \sum_{A\in I}\rho_A(t)N_A(\boldsymbol{x}), \qquad w_h^1(\boldsymbol{x},t) = \sum_{A\in I} w_A^1 N_A(\boldsymbol{x}), \tag{68}
$$

$$
\boldsymbol{u}_h(\boldsymbol{x},t) = \sum_{A\in I}\boldsymbol{u}_A(t)N_A(\boldsymbol{x}), \qquad \boldsymbol{w}_h^2(\boldsymbol{x},t) = \sum_{A\in I} \boldsymbol{w}_A^2 N_A(\boldsymbol{x}), \tag{69}
$$

$$
\Upsilon_h(\boldsymbol{x},t) = \sum_{A\in I}\Upsilon_A(t)N_A(\boldsymbol{x}), \qquad w_h^3(\boldsymbol{x},t) = \sum_{A\in I} w_A^3 N_A(\boldsymbol{x}), \tag{70}
$$

$$
c_h(\boldsymbol{x},t) = \sum_{A\in I} c_A(t)N_A(\boldsymbol{x}), \qquad w_h^4(\boldsymbol{x},t) = \sum_{A\in I} w_A^4 N_A(\boldsymbol{x}), \tag{71}
$$

In Eqs. (68) – (71), the N_A's are a set of basis functions defined on Ω and I is their global-index set. By taking the N_A's as globally C^1-continuous functions, we can define conforming discrete spaces that make the variational formulation well defined.

4.5. Time discretization and numerical implementation

In this section, we present the time integration algorithm for the semi-discrete Eq. (67). We employ the generalized-α method, which was originally proposed by Chung and Hulbert [79] for the equations of structural dynamics, and subsequently extended to the equations of fluid mechanics by Jansen et al. [87]. This method has also been successfully applied in other fields as fluid-structure interaction [88–90] and phase-field modeling [29, 45, 50].

4.5.1. Time stepping scheme

Let $\boldsymbol{V}$ denote the vector of control variable degrees of freedom and let $\dot{\boldsymbol{V}}$ be its time derivative. We define the residual vectors

$$\boldsymbol{R}^{cont} = \{R_A^{cont}\}, \tag{72}$$
$$\boldsymbol{R}^{mom} = \{R_{A,i}^{mom}\}, \tag{73}$$
$$\boldsymbol{R}^{aux} = \{R_A^{aux}\}, \tag{74}$$
$$\boldsymbol{R}^{surf} = \{R_A^{surf}\}, \tag{75}$$

where A is a control-variable index and i is an index associated to the spatial dimensions. The residual components are defined as

$$R_A^{cont} = B(\{N_A, 0, 0, 0\}, \{\rho_h, \boldsymbol{u}_h, \Upsilon_h, c_h\}), \tag{76}$$
$$R_{A,i}^{mom} = B(\{0, N_A\boldsymbol{e}_i, 0, 0\}, \{\rho_h, \boldsymbol{u}_h, \Upsilon_h, c_h\}), \tag{77}$$
$$R_A^{aux} = B(\{0, 0, N_A, 0\}, \{\rho_h, \boldsymbol{u}_h, \Upsilon_h, c_h\}), \tag{78}$$
$$R_A^{surf} = B(\{0, 0, 0, N_A\}, \{\rho_h, \boldsymbol{u}_h, \Upsilon_h, c_h\}), \tag{79}$$

where $\boldsymbol{e}_i$ is the ith cartesian basis vector. The time stepping scheme can be stated as follows: Given the discrete approximation to the global vectors of control variables at time t_n, namely, $\boldsymbol{V}_n$, $\dot{\boldsymbol{V}}_n$ and the current time step $\Delta t = t_{n+1} - t_n$ find $\boldsymbol{V}_{n+1}$ and $\dot{\boldsymbol{V}}_{n+1}$ such that

$$\boldsymbol{R}^{cont}(\boldsymbol{V}_{n+\alpha_f}, \dot{\boldsymbol{V}}_{n+\alpha_m}) = 0, \tag{80}$$
$$\boldsymbol{R}^{mom}(\boldsymbol{V}_{n+\alpha_f}, \dot{\boldsymbol{V}}_{n+\alpha_m}) = 0, \tag{81}$$
$$\boldsymbol{R}^{aux}(\boldsymbol{V}_{n+\alpha_f}, \dot{\boldsymbol{V}}_{n+\alpha_m}) = 0, \tag{82}$$
$$\boldsymbol{R}^{surf}(\boldsymbol{V}_{n+\alpha_f}, \dot{\boldsymbol{V}}_{n+\alpha_m}) = 0, \tag{83}$$

$$\boldsymbol{V}_{n+1} = \boldsymbol{V}_n + \Delta t((1-\gamma)\dot{\boldsymbol{V}}_n + \gamma\dot{\boldsymbol{V}}_{n+1}), \tag{84}$$

where

$$\boldsymbol{V}_{n+\alpha_f} = \boldsymbol{V}_n + \alpha_f\left(\boldsymbol{V}_{n+1} - \boldsymbol{V}_n\right), \tag{85}$$
$$\dot{\boldsymbol{V}}_{n+\alpha_m} = \dot{\boldsymbol{V}}_n + \alpha_m\left(\dot{\boldsymbol{V}}_{n+1} - \dot{\boldsymbol{V}}_n\right), \tag{86}$$

The parameters α_f, α_m and γ are chosen as in [45] to ensure second-order accuracy and unconditional stability of the time-integration algorithm. The non-linear system of equations (80)–(83) may be approximated by using a Newton-Raphson method, which leads to the following two-stage predictor-multicorrector algorithm.

Predictor stage: We adopt a constant-velocity predictor, that is,

$$\boldsymbol{V}_{n+1}^{(0)} = \boldsymbol{V}_n, \tag{87}$$
$$\dot{\boldsymbol{V}}_{n+1}^{(0)} = \frac{\gamma - 1}{\gamma}\dot{\boldsymbol{V}}_n, \tag{88}$$

where the superscript with parentheses denotes the nonlinear iteration index.

Multicorrector stage: Repeat the following steps for $i = 1, 2, ..., i_{max}$ or until convergence

1. Evaluate solution iterates at the α-levels

$$\boldsymbol{V}_{n+\alpha_f}^{(i)} = \boldsymbol{V}_n + \alpha_f\left(\boldsymbol{V}_{n+1}^{(i-1)} - \boldsymbol{V}_n\right), \tag{89}$$
$$\dot{\boldsymbol{V}}_{n+\alpha_m}^{(i)} = \dot{\boldsymbol{V}}_n + \alpha_m\left(\dot{\boldsymbol{V}}_{n+1}^{(i-1)} - \dot{\boldsymbol{V}}_n\right). \tag{90}$$

2. Use the solutions at the α-levels to assemble the residual and the tangent matrix of the linear system

$$\frac{\partial \boldsymbol{R}^{cont}_{(i)}}{\partial \dot{\boldsymbol{V}}_{n+1}} \Delta \dot{\boldsymbol{V}}^{(i)}_{n+1} = -\boldsymbol{R}^{cont}_{(i)}, \tag{91}$$

$$\frac{\partial \boldsymbol{R}^{mom}_{(i)}}{\partial \dot{\boldsymbol{V}}_{n+1}} \Delta \dot{\boldsymbol{V}}^{(i)}_{n+1} = -\boldsymbol{R}^{mom}_{(i)}, \tag{92}$$

$$\frac{\partial \boldsymbol{R}^{aux}_{(i)}}{\partial \dot{\boldsymbol{V}}_{n+1}} \Delta \dot{\boldsymbol{V}}^{(i)}_{n+1} = -\boldsymbol{R}^{aux}_{(i)}, \tag{93}$$

$$\frac{\partial \boldsymbol{R}^{surf}_{(i)}}{\partial \dot{\boldsymbol{V}}_{n+1}} \Delta \dot{\boldsymbol{V}}^{(i)}_{n+1} = -\boldsymbol{R}^{surf}_{(i)}. \tag{94}$$

The resulting linear system is solved using a preconditioned GMRES algorithm [91]. In particular, as preconditioner we have used an incomplete LU factorization. For the numerical examples presented here, solving the linear system with a tolerance of 10^{-5} requires normally 30 to 40 GMRES iterations.

3. Use $\Delta \dot{\boldsymbol{V}}^{(i)}_{n+1}$ to update the iterates as

$$\dot{\boldsymbol{V}}^{(i)}_{n+1} = \dot{\boldsymbol{V}}^{(i-1)}_{n+1} + \Delta \dot{\boldsymbol{V}}^{(i)}_{n+1}, \tag{95}$$

$$\boldsymbol{V}^{(i)}_{n+1} = \boldsymbol{V}^{(i-1)}_{n+1} + \gamma \Delta t \Delta \dot{\boldsymbol{V}}^{(i)}_{n+1}, \tag{96}$$

This completes one nonlinear iteration. The nonlinear iterative algorithm should be repeated until the norm of each of the residual vectors defined in (72)–(75) has been reduced to a given tolerance ϵ_r of its value using the predictions defined in (87)-(88). In this work, we use $\epsilon_r = 10^{-4}$. For the examples presented herein, this typically requires two to four nonlinear iterations.

5. Numerical examples

In this section we present a series of numerical examples that illustrate the predictive ability of our model and the effectiveness of our computational method. The first group of numerical examples shows how surface tension relates with the parameters of the problem and how our model succeeds in reproducing the way in which surfactants lower surface tension. The second simulation demonstrates that surfactants are naturally trapped at liquid-vapor interfaces in accordance with the physical behavior of surface active agents. For this example, we also plot the evolution of the free energy with respect to time, showing that it decreases monotonically as it was imposed in the derivation of the theory. Subsequently, we present a numerical simulation in which a drop of water is being attached to a solid boundary. The aim is to point out that our theory easily allows to model how the contact angle between the liquid-vapor interface and the boundary is modified due to the presence of the surfactant. The last example involves the three-dimensional coalescence of two vapor bubbles. For all the examples, we neglect body forces taking $\boldsymbol{f} = 0$ in Eq. (13). In order to test our code for NSK with surfactants, we have also run several numerical computations (not included in the manuscript) taking the surfactant concentration to zero in the residual. Then, we have verified that these results agree with overkill numerical solutions to the NSK equations. We have also repeated these computations adding the surfactant equation to the residual, but taking very small values for β. In all cases, we achieved the expected results.

All the parameters and the results presented in Section 5 are given in non-dimensional form. We have rescaled the units of measurement of length, mass, time and temperature by L_0, bL_0^3, $L_0/\sqrt{ab}$ and θ_c, respectively, where $L_0 = 1$ denotes a length scale of the computational domain size. Using this non-dimensionalization, it may be shown that the dynamics of the governing equations are controlled by four dimensionless numbers,

$$Re = \frac{L_0 b \sqrt{ab}}{\bar{\mu}}, \quad Ca = \frac{\sqrt{\lambda_{min}/a}}{L_0}, \quad Ba = \frac{\alpha}{ab^2}, \quad Pe = \frac{L_0 \sqrt{ab}}{\kappa \alpha}, \tag{97}$$

where Re is the Reynolds number, Ca denotes the capillary number, Ba is the non-dimensional form of α and Pe is the Peclet number. The capillary number Ca and the Reynolds number Re were chosen according to the methodology

proposed in [45], which relates these parameters to the computational mesh. The objective of this upscaling method is to obtain the largest Reynolds number and the lowest capillary number that can be resolved by a particular mesh. To this end, in [45] the authors propose to scale Ca and Re as

$$Ca = \hbar/L_0 \quad \text{and} \quad Re = \phi L_0/\hbar, \tag{98}$$

where $\hbar$ is a characteristic length scale of the spatial mesh and ϕ is an $O(1)$ constant. We have adopted $\phi = 2$ for all the computations. The reader is referred to [45] for further details about this method.

Remarks

1. Note that Eqs. (97) and (98) imply that λ_{min} is related to the mesh size $\hbar$ by the expression $\lambda_{min} = a\hbar^2$.
2. Note also that the interface thickness $\sqrt{\lambda/a}$ depends on the surfactant concentration through the relation $\sqrt{\lambda/a} = \sqrt{\lambda_{min} g(c)/a} = \hbar\sqrt{g(c)}$.

5.1. Surface tension in the proposed model

It is already known the way surface tension and the NSK parameters are related (see, for example, [61]). In particular, the effect of surface tension σ_{LV} is implicitly included in the NSK model by the relation

$$\sigma_{LV} \simeq K_0\sqrt{\lambda}, \tag{99}$$

where K_0 is a nonlinear function of θ. Eq. (99) is accurate for values of the temperature close to the critical temperature θ_c. Our goal is to show that (99), or equivalently, the non-dimensional form

$$\gamma_{LV} \simeq k_0 Ca\sqrt{g(c)} \tag{100}$$

stands approximately for the NSK model with surfactants, where γ_{LV} is the non-dimensional surface tension, k_0 is a constant for a given temperature and $g(c)$ has been defined right after Eq. (58). With this purpose, we have carried out a number of numerical simulations (each point in Fig. 3 represents a computation) for different initial conditions of the surfactant. In all cases, the initial configuration for the density was the same, namely, it consisted in two vapor bubbles of radius $R_1 = 0.17$ and $R_2 = 0.1$ centered at $C_1 = (0.35, 0.5)$ and $C_2 = (0.75, 0.5)$, respectively. The initial values of the density for the liquid and the vapor phases were those corresponding to the Maxwell states[3]. As expected, the two bubbles merge into one circular vapor area, whose radius is given by the temperature (see, e.g., [45]). The initial density condition does not have an impact on the scaling that we want to analyze, so the study could be repeated with different density initial conditions and the results would not be altered. For the surfactant, we have employed in all cases a flat initial condition representing a constant surfactant concentration. Different simulations employed different values of the constant so as to vary the right-hand side of Eq. (100). In each simulation we have waited for the steady state and then we have measured the radius r of the resulting bubble and the pressure difference Δp between the liquid and the vapor phases. Then, we have used the two dimensional form of Young-Laplace equation

$$\Delta p = \frac{\gamma_{LV}}{r}, \tag{101}$$

to define an estimate of surface tension at the liquid-vapor interface, that is, $\gamma_{LV} = r\Delta p$. Finally, we have plotted (see Fig. 3) our estimate of suface tension with respect to $Ca\sqrt{g(c)}$. This procedure was carried out for two different temperatures, $\theta = 0.7$ and $\theta = 0.85$.

[3] The Maxwell States for the liquid (ρ_l^M) and the vapor phases (ρ_v^M) employed in the numerical examples of Sect. 5.1 are those listed below:

θ	ρ_v^M	ρ_l^M
0.85	0.10	0.60
0.7	0.04	0.71

The computational domain, $\Omega = (0,1)^2$, was comprised of 128 $\mathcal{C}^1$-quadratic elements in each direction. We adopted periodic boundary conditions. The other parameters employed in these computations are $Re = 256$, $Ca = 0.0078125$, $Ba = 0.1$ and $Pe = 500$. The time step used was constant and equal to $\Delta t = 0.01$.

As it can be seen in Fig. 3, the surface tension follows approximately a linear relation with the values of the capillarity function at the interface. This proves that the parameter k_0 remains constant in our model for given temperatures close to the critical temperature θ_c. Thus, the expression (100) is valid for the theory presented herein. We have also plotted our estimate of surface tension with respect to the surfactant concentration at the interface (see inset in Fig.(3)), which makes evident that surface tension decreases with surfactant concentration. This is in agreement with the behavior of most of the surfactants employed in the chemical industry.

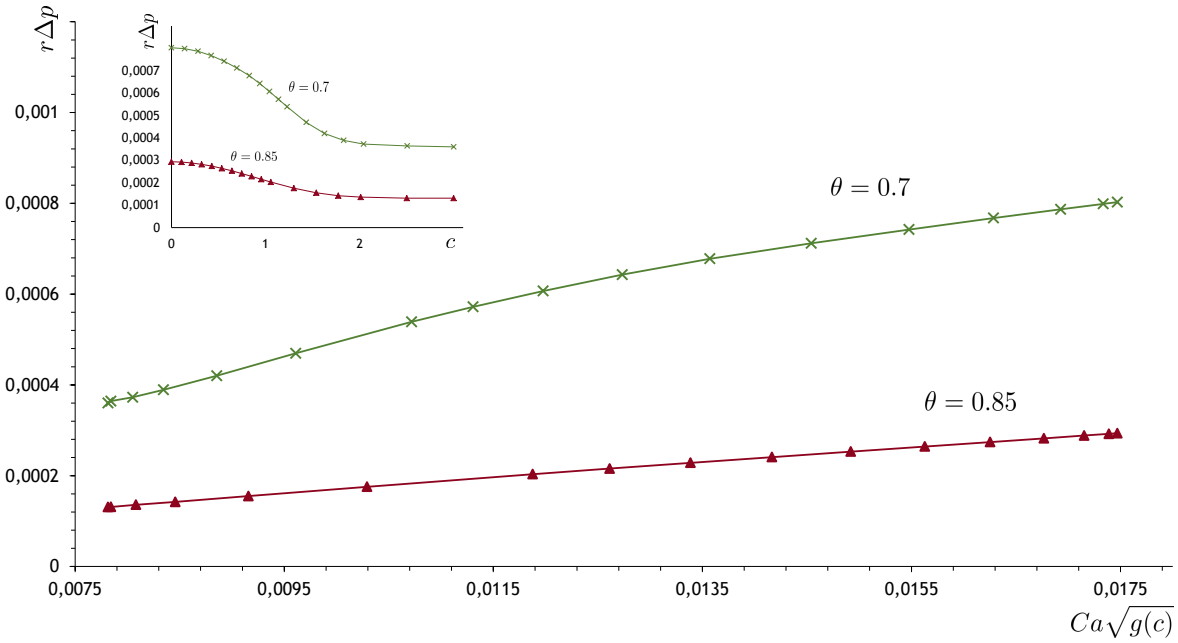

Figure 3: Non-dimensional plot of our estimate of surface tension $r\Delta p$ as a function of capillarity for two different temperatures. For the steady state, surface tension scales almost linearly with the values of the capillarity function at the interface. In the inset we also plot surface tension as a funcion of the surfactant concentration at the interface. Note that surface tension decreases with surfactant concentration.

5.2. Trapping of surfactant at the liquid-vapor interface

This numerical example shows how our model naturally predicts the trapping of the surfactant at the liquid-vapor interface. As shown in the previous example, the surfactant can also change the properties of the interface, which, in turn may alter the dynamics of the system, for example, inhibiting partially or completely the coalescence of vapor bubbles. This example illustrates both phenomena. Finally, we also use this computation to show that the free-energy defined in Eq. (9) decreases along solutions to the governing equations. We have carried out a numerical simulation predicting the dynamics of three vapor bubbles (see left column in Fig. 4) using the traditional NSK model without surfactants (see [45] for further details). Then, we repeated exactly the same simulation with the theory presented herein (middle and right columns in Fig. 4).

Three bubbles of radius $R_1 = 0.11$, $R_2 = 0.18$ and $R_3 = 0.08$ were initially centered at $C_1 = (0.25, 0.45)$, $C_2 = (0.65, 0.45)$ and $C_3 = (0.51, 0.70)$. The initial condition for the density variable [see Figs. 4(a) and 4(b)] inside and outside of the bubbles was that corresponding to the Maxwell states of the vapor (red color) and the liquid water (blue color), respectively, for a temperature $\theta = 0.85$, that is, $\rho_v^M = 0.10$ and $\rho_l^M = 0.60$. We have used a uniform mesh comprised of 512 $\mathcal{C}^1$-quadratic elements in each direction and we have imposed periodic boundary conditions. In both simulations we have employed $Re = 1024$ and $Ca = 0.001953125$. For the NSK theory with surfactant we

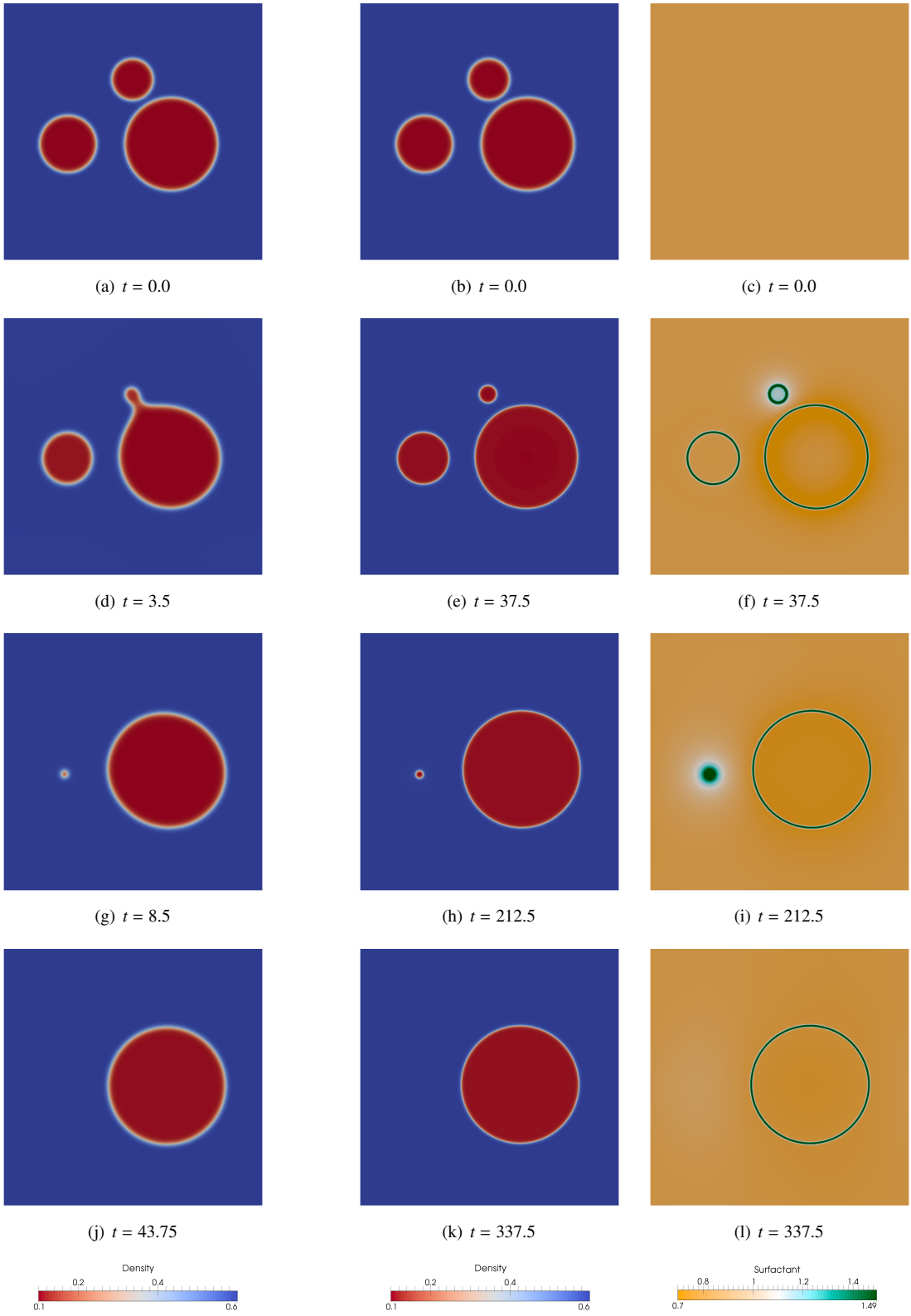

(a) $t = 0.0$ (b) $t = 0.0$ (c) $t = 0.0$

(d) $t = 3.5$ (e) $t = 37.5$ (f) $t = 37.5$

(g) $t = 8.5$ (h) $t = 212.5$ (i) $t = 212.5$

(j) $t = 43.75$ (k) $t = 337.5$ (l) $t = 337.5$

Figure 4: Simulation of three vapor bubbles using the NSK theory without surfactant (left column) and with surfactant (middle and right columns). In both cases, we use a square-shaped domain $\Omega = (0, 1)^2$ composed of 512^2 elements. The initial configuration consists in three vapor bubbles [red color in the density plots (a) and (b)] deposited on a liquid matrix (blue color). For the NSK theory with surfactant we also adopt as initial condition an homogeneous distribution of the surfactant concentration, namely, $c_0 = 0.8$. Comparing the density plots of both theories (left and middle columns) we can see that the NSK model with surfactant inhibits the coalescence of the small and big bubbles. Since the surfactant is attracted by the areas with higher density gradients, the surfactant concentration increases at the interfaces (green color in the surfactant plots). The parameters used in these simulations are $Re = 1024$, $Ca = 0.001953125$, $Ba = 0.005$ and $Pe = 10000$.

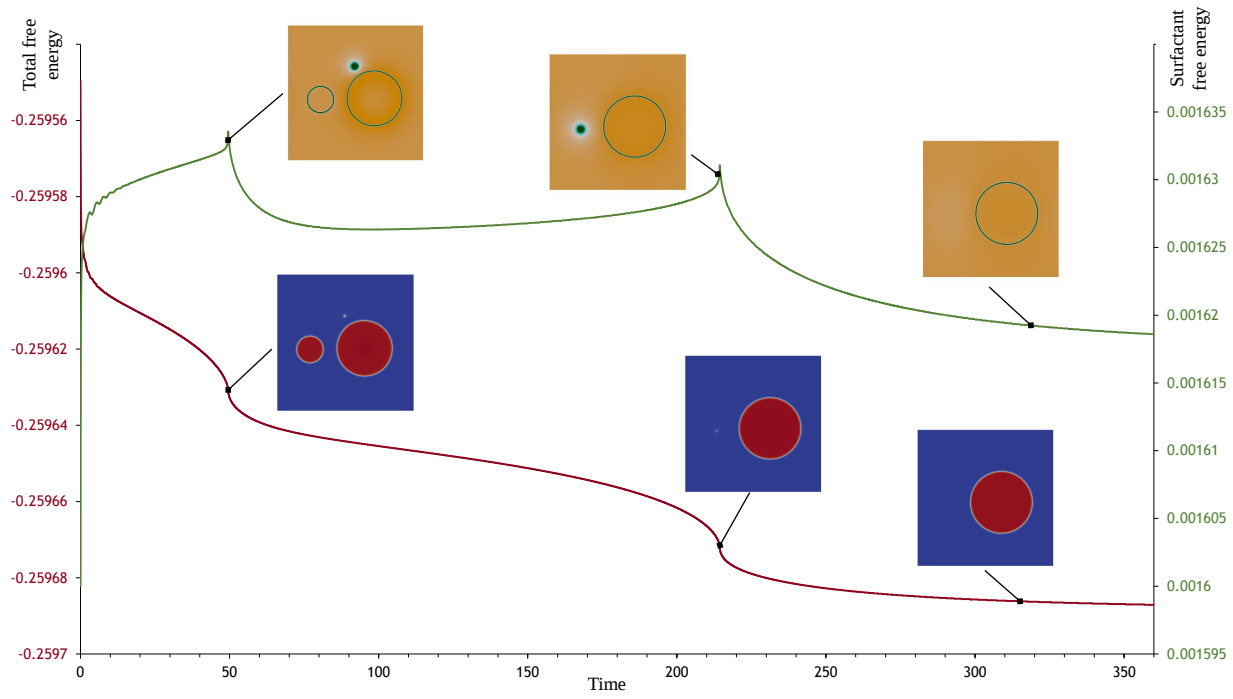

Figure 5: Plot of the total free energy of the system (red color) and the surfactant free energy $\mathcal{U}$ (green color) with respect to time. The total energy is a monotonically decreasing function in agreement with the conditions imposed during the derivation of our model. The surfactant energy reaches two peaks in the moments previous to the collapse of the smaller bubbles. Initially, the surfactant concentration is uniform. We have used the parameters $Re = 1024$, $Ca = 0.001953125$, $Ba = 0.005$ and $Pe = 10000$.

have adopted $Ba = 0.005$ and $Pe = 10000$. Initially, the surfactant [see Fig. 4(c)] was evenly distributed on the whole domain so that the initial surfactant concentration was the constant $c_0 = 0.8$. In both cases, we used a constant time step equal to $\Delta t = 0.00125$.

In Fig. 4 we plot the evolution of the density for the NSK theory (left column) and the evolution of the density and surfactant concentration for the NSK theory with surfactant (middle and right columns) for different time steps until a steady state is reached. As it can be seen, in the simulation without surfactants, the bubbles that are closer are able to coalesce [Fig. 4(d)]. However, the presence of the surfactant can inhibit the coalescence of these two bubbles [Fig. 4(e)], altering the behavior of the system. The surfactant is attracted by the regions with a higher density gradient, that is, the interfaces between the vapor and the liquid phases (see the right column of Fig. 4). This is in agreement with the physical behavior of surface active agents.

Fig. 5 (red line) shows the time evolution of the free-energy of the system [see Eq. (9)], which is monotonically decreasing as predicted by the theory. For further insight into the model, we also plot the evolution of the free energy corresponding to the surfactant (green line), that is, $\mathcal{U}$ in Eq. (46). There is no reason why we should expect $\mathcal{U}$ to be a decreasing function of time, and, in fact, it is not. One can observe two sharp increases in the surfactant free energy at times $t \simeq 50$ and $t \simeq 215$, which coincide with the previous instants to the disappearance of each of the bubbles [see Figs. 4(h) and 4(i)]. When bubbles collapse, the surfactant gets trapped in smaller areas and therefore, achieves higher concentrations. The oscillatory behavior of the surfactant free energy at early stages ($t < 20$) is caused by the initial conditions[4]. The initial condition for the surfactant is a flat function representing a constant value. The surfactant gets quickly trapped at the interfaces and produces strong dynamics at early times, which manifests itself with small-amplitude oscillations in the surfactant free energy.

[4]We have repeated the computation with a time step four times smaller to make sure that the oscillatory behavior was not a consequence of the discretization errors.

5.3. Attachment of a drop of water to a wall

In all the previous simulations we have imposed periodic boundary conditions. However, in this case we will try to emulate how the presence of the surfactant may modify the contact angle φ between a drop of water and a solid substrate. For ideal solid surfaces, where the solid is flat and rigid, the equilibrium contact angle φ_E between the liquid-vapor interface and the boundary is given by Young equation, that is,

$$\gamma_{SL} + \gamma_{LV}\cos(\varphi_E) = \gamma_{SV} \tag{102}$$

where γ_{SV} and γ_{SL} are the surface tension at the solid-vapor interface and at the solid-liquid interface, respectively. Young's relation (102) and expression (100) allow us to approximate the contact angle φ as

$$\cos(\varphi) \simeq \frac{\gamma_{SV} - \gamma_{SL}}{\gamma_{LV}} \simeq \frac{\varepsilon}{Ca\sqrt{g(c)}} \tag{103}$$

where we consider $\varepsilon = \dfrac{\gamma_{SV} - \gamma_{SL}}{k_0}$ as a positive constant. Therefore, the boundary condition (61) becomes

$$\nabla\rho \cdot \boldsymbol{n} = |\nabla\rho| \frac{\varepsilon}{Ca\sqrt{g(c)}} \tag{104}$$

Analogously, (62) takes on the form

$$\nabla c \cdot \boldsymbol{n} = |\nabla c| \frac{\varepsilon}{Ca\sqrt{g(c)}} h(\rho) \tag{105}$$

where $h(\rho)$ is given by (64).

In order to illustrate the effectiveness of our model we have carried out the following numerical simulation (see Fig. 6). A drop of liquid water [blue color in Fig. 6(a)] is initially located close to a solid boundary where we are imposing (104) and (105). In the horizontal direction we adopt periodic boundary conditions. The computational domain is a rectangle $\Omega = (0, 1.0) \times (0, 0.5)$ and the computational mesh is uniform and composed of 256×128 C^1-quadratic elements. Initially, the water droplet has a radius $R = 0.12$ and is centered at $C = (0.5, 0.15)$. For the initial values of the density in the liquid and the vapor phase we use the Maxwell States at $\theta = 0.85$, that is, $\rho_l^M = 0.60$ and $\rho_v^M = 0.10$. The initial distribution for the surfactant is the one indicated in Fig. 6(b) and it consists of a drop of surfactant of radius $R_s = 0.05$ (green color) located near to the upper boundary, more specifically, centered at $C_s = (0.5, 0.4)$. Note that the water droplet is attracted by the lower boundary due to the capillary forces [see Fig.6(e)], as we have neglected gravity forces. The parameters used in this numerical example are $Re = 512$, $Ca = 0.00390625$, $Ba = 0.04$, $Pe = 125$ and $\varepsilon = 0.003845215$. The time step was constant and equal to $\Delta t = 0.0001$. From Eq. (104), it is obvious that different initial conditions for the surfactant would lead to different static contact angles. This phenomena is very important to control wettability with surfactants in practical applications.

5.4. Coalescence of vapor bubbles in three dimensions

This example shows the details of two coalescing bubbles with surfactants in three dimensions (see Fig. 7). The computational domain is the cube $\Omega = (0, 1)^3$ which is discretized with 128 C^1-quadratic elements in each direction. The two vapor bubbles have a radius $R_1 = 0.12$ and $R_2 = 0.25$ and they are initially centered at $C_1 = (0.35, 0.57, 0.5)$ and $C_2 = (0.70, 0.40, 0.50)$. The initial values of the density for the liquid and the vapor phases are those corresponding to the Maxwell states at $\theta = 0.85$, that is, $\rho_l^M = 0.60$ and $\rho_v^M = 0.10$. For the surfactant [see Fig.7(a)], we have adopted a constant initial condition, namely, $c_0 = 0.8$. The rest of the parameters are $Re = 256$, $Ca = 0.0078125$, $Ba = 0.01$, $Pe = 1000$ and $\Delta t = 0.005$. We impose periodic boundary conditions in all directions.

In order to facilitate the visualization of the results in the surfactant plot (see Fig. 7), we have made a clip of the cubic domain. Moreover, we are plotting an isocontour surface of the density (grey color) which represents the liquid-vapor interface so that we can know where the bubbles are located. As in the previous examples, the surfactant (green color in Fig. 7) is trapped by the regions with a higher density gradient, that is, the liquid-vapor interfaces (grey color).

6. Conclusions

We propose a model for single-component, two-phase flow with surfactants. The fluid naturally undergoes phase-transformations between vapor and liquid states. The model is derived from a free-energy functional using the thermodynamics framework and successfully predicts important features of two-phase flow with surfactants. For example, the model predicts that the surfactant reduces the liquid-vapor surface tension and is naturally trapped at the interface, as observed in experiments.

The discretization of the model poses significant challenges for classical numerical algorithms due to the presence of higher-order derivatives, stiffness in space and time an the existence of moving interfaces. We propose a computational method based on Isogeometric Analysis that leads to an efficient and accurate numerical solution.

Finally, we show the viability of our theoretical framework and numerical algorithm by showcasing several examples of vapor bubble dynamics in two and three dimensions. We believe our model has significant potential to study the influence of surfactants on phase transformations. In the future, we plan to extend it to the non-isothermal case.

Acknowledgements

HG was partially supported by the European Research Council through the FP7 Ideas Starting Grant Program (Contract #307201). HG and JB were partially supported by Xunta de Galicia, co-financed with FEDER funds. The authors are also grateful to Prof. Uwe Thiele for valuable discussions.

References

[1] A. Singh, J. V. Hamme, O. Ward, Surfactants in microbiology and biotechnology: Part 2. Application aspects, Biotechnology Advances 25 (2007) 99 – 121.

[2] J. Van Hamme, A. Singh, O. Ward, Surfactants in microbiology and biotechnology: Part 1. Physiological aspects, Biotechnology Advances 24 (2006) 604–620.

[3] M. Rosen, Surfactants in Emerging Technology, Surfactant Science, Taylor & Francis, 1987.

[4] Q. Tang, Y. Chan, N. Wong, R. Cheung, Surfactant-assisted processing of polyimide/multiwall carbon nanotube nanocomposites for microelectronics applications, Polymer International 59 (2010) 1240–1245.

[5] A. Florence, J. Gillan, Biological implications of the use of surfactants in medicines: and the biphasic effects of surfactants in biological systems, Pesticide Science 6 (1975) 429–439.

[6] L. Rodrigues, I. Banat, J. Teixeira, R. Oliveira, Biosurfactants: potential applications in medicine, Journal of Antimicrobial Chemotherapy 57 (2006) 609–618.

[7] R. King, Pulmonary surfactant, Journal of Applied Physiology 53 (1982) 1–8.

[8] H. Halliday, Surfactants: past, present and future, Journal of perinatology 28 (2008) S47–S56.

[9] S. Anna, H. Mayer, Microscale tipstreaming in a microfluidic flow focusing device, Physics of Fluids 18 (2006) –.

[10] L. Leal, Flow induced coalescence of drops in a viscous fluid, Physics of Fluids 16 (2004) 1833–1851.

[11] A. Pereira, P. M. J. Trevelyan, U. Thiele, S. Kalliadasis, Dynamics of a horizontal thin liquid film in the presence of reactive surfactants, Physics of Fluids 19 (2007).

[12] H. Stone, L. Leal, The effects of surfactants on drop deformation and breakup, Journal of Fluid Mechanics 220 (1990) 161–186.

[13] U. Thiele, A. J. Archer, M. Plapp, Thermodynamically consistent description of the hydrodynamics of free surfaces covered by insoluble surfactants of high concentration, Physics of Fluids 24 (2012) 102–107.

[14] R. Farn, Chemistry and Technology of Surfactants, Wiley, 2008.

[15] D. Myers, An Overview of Surfactant Science and Technology, John Wiley & Sons, Inc., 2005, pp. 1–28.

[16] M. Rosen, Characteristic Features of Surfactants, John Wiley & Sons, Inc., 2004, pp. 1–33.

[17] S. Aland, A. Voigt, Simulation of common features and differences of surfactant-based and solid-stabilized emulsions, Colloids and Surfaces A: Physicochemical and Engineering Aspects 413 (2012) 298–302.

[18] H. Garcke, K. Lam, B. Stinner, Diffuse interface modelling of soluble surfactants in two-phase flow, Communications in Mathematical Sciences 12 (2014) 1475–1522.

[19] M. Muradoglu, G. Tryggvason, A front-tracking method for computation of interfacial flows with soluble surfactants, Journal of computational physics 227 (2008) 2238–2262.

[20] C. Teng, I. Chern, M. Lai, Simulating binary fluid-surfactant dynamics by a phase field model, Discrete and Continuous Dynamical Systems - Series B 17 (2012) 1289–1307.

[21] R. van der Sman, S. van der Graaf, Diffuse interface model of surfactant adsorption onto flat and droplet interfaces, Rheologica Acta 46 (2006) 3–11.

[22] H. Ceniceros, The effects of surfactants on the formation and evolution of capillary waves, Physics of Fluids 15 (2003) 245–256.

[23] M. A. Drumright-Clarke, Y. Renardy, The effect of insoluble surfactant at dilute concentration on drop breakup under shear with inertia, Physics of Fluids 16 (2004) 14–21.

[24] A. James, J. Lowengrub, A surfactant-conserving volume-of-fluid method for interfacial flows with insoluble surfactant, Journal of Computational Physics 201 (2004) 685–722.

[25] S. Engblom, M. Do-Quang, G. Amberg, A. Tornberg, On diffuse interface modeling and simulation of surfactants in two-phase fluid flow, Communications in Computational Physics 14 (2013) 879–915.
[26] S. Khatri, A.-K. Tornberg, An embedded boundary method for soluble surfactants with interface tracking for two-phase flows, Journal of Computational Physics 256 (2014) 768 – 790.
[27] H. Liu, Y. Zhang, Phase-field modeling droplet dynamics with soluble surfactants, Journal of Computational Physics 229 (2010) 9166 – 9187.
[28] J. Crank, Free and Moving Boundary Problems, Oxford science publications, Clarendon Press, 1987.
[29] H. Gomez, V. Calo, Y. Bazilevs, T. Hughes, Isogeometric Analysis of the Cahn-Hilliard phase-field model, Computer Methods in Applied Mechanics and Engineering 197 (2008) 43334352.
[30] H. Gomez, T. Hughes, Provably unconditionally stable, second-order time-accurate, mixed variational methods for phase-field models, Journal of Computational Physics 230 (2011) 5310–5327.
[31] H. Gomez, A. Reali, G. Sangalli, Accurate, efficient, and (iso) geometrically flexible collocation methods for phase-field models, Journal of Computational Physics 262 (2014) 153–171.
[32] J. Liu, H. Gomez, J. Evans, T. Hughes, C. Landis, Functional entropy variables: A new methodology for deriving thermodynamically consistent algorithms for complex fluids, with particular reference to the isothermal Navier-Stokes-Korteweg equations, Journal of Computational Physics 248 (2013) 47–86.
[33] G. Caginalp, Stefan and hele-shaw type models as asymptotic limits of the phase-field equations, Physical Review A 39 (1989) 5887–5896.
[34] R. Kobayashi, A numerical approach to three-dimensional dendritic solidification, Experimental Mathematics 3 (1994) 59–81.
[35] O. Penrose, P. Fife, Thermodynamically consistent models of phase-field type for the kinetic of phase transitions, Physica D: Nonlinear Phenomena 43 (1990) 44 – 62.
[36] I. Fonseca, M. Morini, V. Slastikov, Surfactants in foam stability: A phase-field model, Archive for Rational Mechanics and Analysis 183 (2007) 411–456.
[37] M. Borden, C. Verhoosel, M. Scott, T. Hughes, C. Landis, A phase-field description of dynamic brittle fracture, Computer Methods in Applied Mechanics and Engineering 217220 (2012) 77 – 95.
[38] J. Jeong, N. Goldenfeld, J. Dantzig, Phase field model for three-dimensional dendritic growth with fluid flow, Physical Review E 64 (2001) 041602.
[39] Y. Kim, N. Provatas, N. Goldenfeld, J. Dantzig, Universal dynamics of phase-field models for dendritic growth, Physical Review E 59 (1999) 2546.
[40] T. Biben, K. Kassner, C. Misbah, Phase-field approach to three-dimensional vesicle dynamics, Physical Review E 72 (2005) 041921.
[41] E. Fried, M. Gurtin, Dynamic solid-solid transitions with phase characterized by an order parameter, Physica D: Nonlinear Phenomena 72 (1994) 287 – 308.
[42] S. Tremaine, On the origin of irregular structure in saturn's rings, The Astronomical Journal 125 (2003) 894.
[43] L. Cueto-Felgueroso, R. Juanes, Nonlocal interface dynamics and pattern formation in gravity-driven unsaturated flow through porous media, Physical Review Letters 101 (2008) 244504.
[44] H. Gomez, L. Cueto-Felgueroso, R. Juanes, Three-dimensional simulation of unstable gravity-driven infiltration of water into a porous medium, Journal of Computational Physics 238 (2013) 217–239.
[45] H. Gomez, T. Hughes, X. Nogueira, V. Calo, Isogeometric Analysis of the isothermal Navier-Stokes-Korteweg equations, Computer Methods in Applied Mechanics and Engineering 199 (2010) 1828–1840.
[46] H. Frieboes, B. Lowengrub, S. Wise, B. Zheng, B. Macklin, E. Bearer, V. C. A, Computer simulation of glioma growth and morphology. Neuroimage 37, NeuroImage (2007) 59–70.
[47] G. Vilanova, I. Colominas, H. Gomez, Capillary networks in tumor angiogenesis: From discrete endothelial cells to phase-field averaged descriptions via isogeometric analysis, International Journal for Numerical Methods in Biomedical Engineering 29 (2013) 1015–1037.
[48] J. Xu, G. Vilanova, H. Gomez, A mathematical model coupling tumor growth and angiogenesis (????). In review.
[49] E. van Brummelen, H. S. Roudbari, G. van Zwieten, Elasto-capillarity simulations based on the Navier-Stokes-Cahn-Hilliard equations, ArXiv 1510.02441v1 (2015) 1– 8.
[50] J. Bueno, C. Bona-Casas, Y. Bazilevs, H. Gomez, Interaction of complex fluids and solids: Theory, algorithms and application to phase-change-driven implosion, Computational Mechanics 55 (2015) 1105–1118.
[51] D. M. Anderson, G. B. McFadden, A. A. Wheeler, Diffuse-interface methods in fluid mechanics, Annual Review of Fluid Mechanics 30 (1998) 139–165.
[52] A. Bray, Theory of phase ordering kinetics, Physica A: Statistical Mechanics and its Applications 194 (1993) 41 – 52.
[53] L. Chen, Phase-field models for microstructure evolution, Annual Review of Materials Research 32 (2002) 113–140.
[54] H. Gomez, K. van der Zee, Encyclopedia of Computational Mechanics. Phase Field Models and Methods, John Wiley & Sons, Ltd, ????
[55] I. Steinbach, Phase-field models in materials science, Modelling Simul. Mater. Sci. Eng. 17 (2009) 073001.
[56] J. Gibbs, On the Equilibrium of Heterogeneous Substances, 1874.
[57] D. Korteweg, Sur la forme que prennent les équations du mouvement des fluides si l'on tient compte des forces capillaires causées par des variations de densité considérables mais continues et sur la théorie de la capillarité dans l'hypothèse d'une variation continue de la densité, Arch. Néerl. (2) 6 (1901) 1–24.
[58] J. van der Waals, The thermodynamic theory of capillarity under the hypothesis of a continuous variation of density, Journal of Statistical Physics 20 (1979) 200–244.
[59] J. Dunn, J. Serrin, On the thermomechanics of interstitial working, Archive for Rational Mechanics and Analysis 88 (1985) 95–133.
[60] L. Tian, Y. Xu, J. Kuerten, J. van der Vegt, A local discontinuous galerkin method for the (non)-isothermal navierstokeskorteweg equations, Journal of Computational Physics 295 (2015) 685 – 714.
[61] D. Diehl, Higher order schemes for simulation of compressible liquid-vapor flows with phase change, Ph.D. thesis, Albert-Ludwigs-Universitat, 2007.
[62] J. Giesselmann, C. Makridakis, T. Pryer, Energy consistent discontinuous galerkin methods for the navier–stokes–korteweg system, Mathe-

matics of Computation 83 (2014) 2071–2099.
[63] J. Liu, C. M. Landis, H. Gomez, T. J. Hughes, Liquid–vapor phase transition: Thermomechanical theory, entropy stable numerical formulation, and boiling simulations, Computer Methods in Applied Mechanics and Engineering 297 (2015) 476 – 553.
[64] T. Hughes, J. Cottrell, Y. Bazilevs, Isogeometric Analysis: CAD, Finite Elements, NURBS, exact geometry and mesh refinement, Computer Methods in Applied Mechanics and Engineering 194 (2005) 4135 – 4195.
[65] Y. Bazilevs, L. Beirão Da Veiga, J. Cottrell, T. Hughes, G. Sangalli, Isogeometric Analysis: Approximation, stability and error estimates for h-refined meshes, Mathematical Models and Methods in Applied Sciences 16 (2006) 1031–1090.
[66] Y. Bazilevs, V. Calo, J. Cottrell, J. Evans, T. Hughes, S. Lipton, M. Scott, T. Sederberg, Isogeometric Analysis using T-splines, Computer Methods in Applied Mechanics and Engineering 199 (2010) 229 – 263.
[67] Y. Bazilevs, V. Calo, Y. Zhang, T. Hughes, Isogeometric Fluid-Structure Interaction analysis with applications to arterial blood flow, Computational Mechanics 38 (2006) 310–322.
[68] J. Cottrell, T. Hughes, A. Reali, Studies of refinement and continuity in Isogeometric structural analysis, Computer Methods in Applied Mechanics and Engineering 196 (2007) 4160 – 4183.
[69] J. Cottrell, A. Reali, Y. Bazilevs, T. Hughes, Isogeometric Analysis of structural vibrations, Computer Methods in Applied Mechanics and Engineering 195 (2006) 5257 – 5296.
[70] H. Casquero, L. Lei, J. Zhang, A. Reali, H. Gomez, Isogeometric collocation using analysis-suitable T-splines of arbitrary degree, Computer Methods in Applied Mechanics and Engineering 301 (2016) 164 – 186.
[71] H. Casquero, L. Lei, Y. Zhang, A. Reali, J. Kiendl, H. Gomez, Arbitrary-degree T-splines for isogeometric analysis of fully nonlinear Kirchhoff-Love shells, submitted for publication (2016).
[72] J. Warren, H. Weimer, Subdivision Methods for Geometric Design: A Constructive Approach, 1st ed., Morgan Kaufmann Publishers Inc., San Francisco, CA, USA, 2001.
[73] M. Borden, T. Hughes, C. Landis, C. Verhoosel, A higher-order phase-field model for brittle fracture: Formulation and analysis within the isogeometric analysis framework, Computer Methods in Applied Mechanics and Engineering 273 (2014) 100 – 118.
[74] J. Bueno, I. Starodumov, H. Gomez, P. Galenko, D. Alexandrov, Three dimensional structures predicted by the modified phase field crystal equation , Computational Materials Science 111 (2016) 310 – 312.
[75] L. Dedè, M. Borden, T. Hughes, Isogeometric analysis for topology optimization with a phase field model, Archives of Computational Methods in Engineering 19 (2012) 427–465.
[76] R. Dhote, H. Gomez, R. Melnik, J. Zu, Isogeometric analysis of coupled thermo-mechanical phase-field models for shape memory alloys using distributed computing, Procedia Computer Science 18 (2013) 1068 – 1076. 2013 International Conference on Computational Science.
[77] H. Gomez, L. De Lorenzis, The variational collocation method, Computer Methods in Applied Mechanics and Engineering (2016).
[78] M. Gurtin, E. Fried, L. Anand, Thermodynamics and constitutive restrictions: The Coleman-Noll procedure, in: The Mechanics and Thermodynamics of Continua, Cambridge University Press, 2010, pp. 232–233. Cambridge Books Online.
[79] J. Chung, G. Hulbert, A time integration algorithm for structural dynamics with improved numerical dissipation: The generalized-α method., Journal of Applied Mechanics 60 (1993) 371–375.
[80] J. Cottrell, T. Hughes, Y. Bazilevs, Isogeometric Analysis: Toward Integration of CAD and FEA, Wiley, 2009.
[81] C. de Boor, On calculating with B-splines, Journal of Approximation Theory 6 (1972) 50 – 62.
[82] M. G. Cox, The numerical evaluation of B-splines, IMA Journal of Applied Mathematics 10 (1972) 134–149.
[83] J. E. Marsden, T. Hughes, Mathematical Foundations of Elasticity, Dover Publications, Inc, 1994.
[84] J. Cahn, J. Hilliard, Free Energy of a Nonuniform System. I. Interfacial Free Energy, John Wiley & Sons, Inc., 2013, pp. 29–38.
[85] J. Liu, Thermodynamically consistent modeling and simulation of multiphase flows, Ph.D. thesis, The University of Texas at Austin, 2014.
[86] F. White, Fluid Mechanics, McGraw-Hill international editions, McGraw-Hill, 2003.
[87] K. Jansen, C. Whiting, G. Hulbert, A generalized-α method for integrating the filtered Navier-Stokes equations with a stabilized Finite Element Method, Computer Methods in Applied Mechanics and Engineering 190 (2000) 305 – 319.
[88] Y. Bazilevs, V. Calo, T. Hughes, Y. Zhang, Isogeometric Fluid-Structure Interaction: Theory, algorithms, and computations, Computational Mechanics 43 (2008) 3–37.
[89] H. Casquero, C. Bona-Casas, H. Gomez, A NURBS-based immersed methodology for fluid-structure interaction, Computer Methods in Applied Mechanics and Engineering 284 (2015) 943–970.
[90] H. Casquero, L. Lei, C. Bona-Casas, J. Zhang, H. Gomez, A hybrid variational-collocation immersed method for fluid-structure interaction using unstructured T-splines, *International Journal for Numerical Methods in Engineering*, Accepted for publication, DOI: 10.1002/nme.5004 (2016).
[91] Y. Saad, M. Schultz, GMRES: A generalized minimal residual algorithm for solving nonsymmetric linear systems, SIAM Journal on Scientific and Statistical Computing 7 (1986) 856–869.

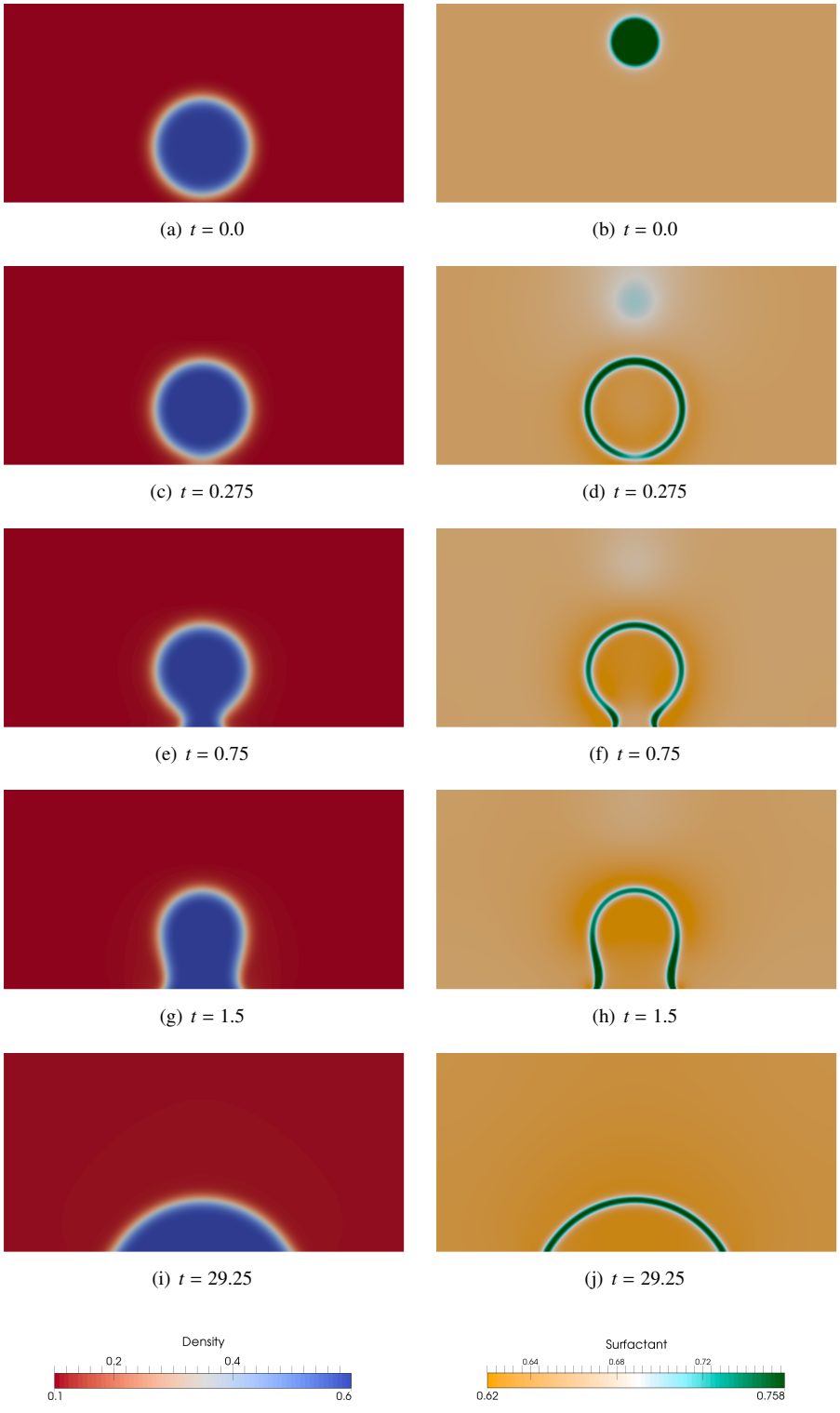

(a) $t = 0.0$ (b) $t = 0.0$

(c) $t = 0.275$ (d) $t = 0.275$

(e) $t = 0.75$ (f) $t = 0.75$

(g) $t = 1.5$ (h) $t = 1.5$

(i) $t = 29.25$ (j) $t = 29.25$

Figure 6: Evolution of density (left) and surfactant concentration (right) for the attachment of a drop of water to a wall. The commputational domain is the rectangle $\Omega = (0, 1.0) \times (0, 0.5)$ and the computational mesh is u¡niform and composed of 256×128 $\mathcal{C}^1$-quadratic elements. Initially, a drop of liquid water (blue color in the density plot) is located close to the lower boundary where we are controlling the contact angle as a function of surfactant concentration. In the horizontal direction we adopt periodic boundary conditions. The surfactant is initially concentrated close to the upper boundary (Fig. 6(b)) though it is rapidly attracted by the liquid/vapor interface (green color in the surfactant plot). The water droplet is attracted by the lower boundary due to the capillary forces (see Fig.6(e)). Note that we are neglecting gravity forces. We have adopted $Re = 512$, $Ca = 0.00390625$, $Ba = 0.04$, $Pe = 125$ and $\varepsilon = 0.003845215$.

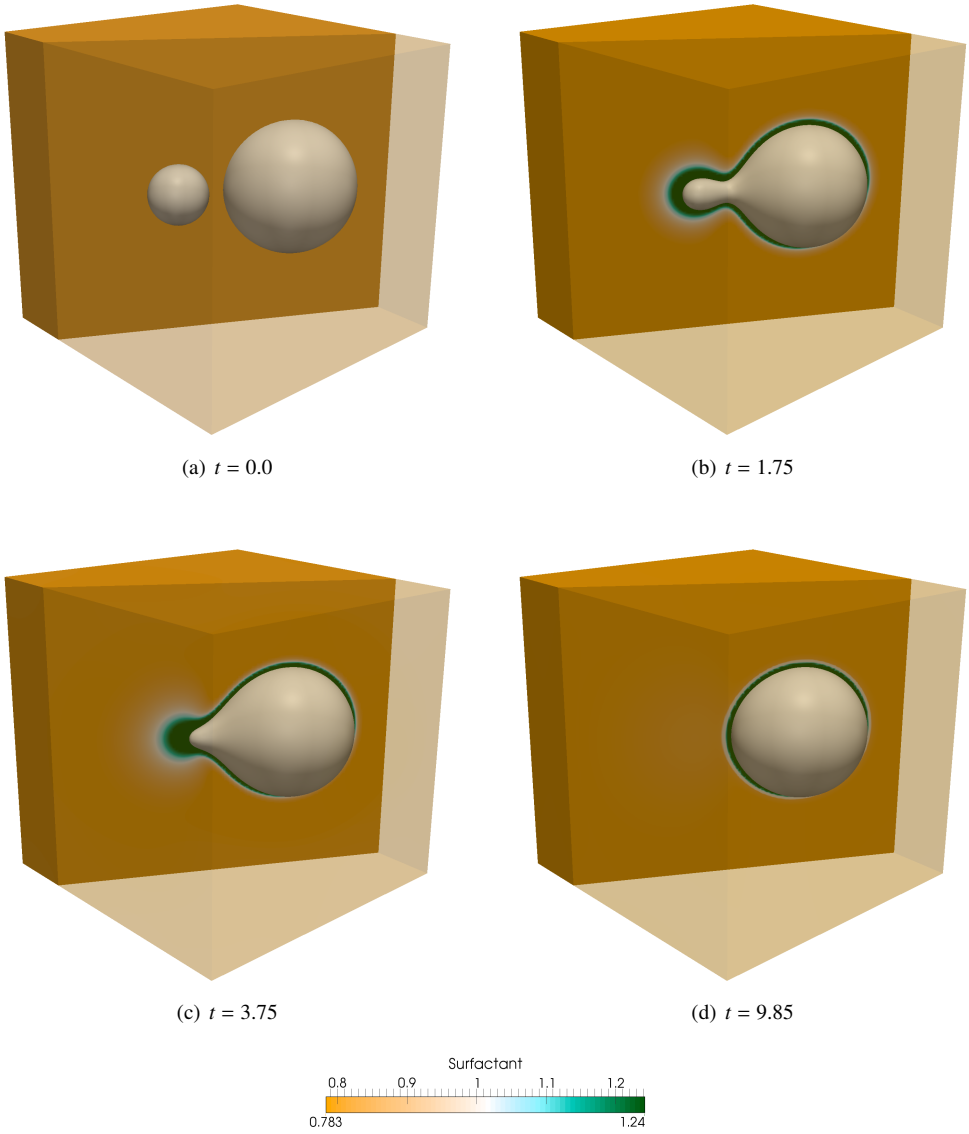

(a) $t = 0.0$ (b) $t = 1.75$

(c) $t = 3.75$ (d) $t = 9.85$

Figure 7: Evolution of surfactant concentration for the three dimensional coalescence of two vapor bubbles. The computational domain is the cube $\Omega = (0, 1)^3$, which is composed of 128^3 C^1-quadratic elements. We impose periodic boundary conditions in all directions. Initially, an homogeneous distribution of the surfactant concentration is adopted (Fig.7(a)), namely, $c_0 = 0.8$. We have made a clip of the geometry to facilitate the visualization of the results. We are plotting an isocontour surface of the density (grey color) which represents the liquid-vapor interface. The surfactant is trapped by the regions with higher density gradients, that is, the liquid-vapor interfaces. We have used the parameters $Re = 256$, $Ca = 0.0078125$, $Ba = 0.01$ and $Pe = 1000$.